


















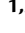


MCU proteins dominate in vivo mitochondrial Ca^{2+} uptake in *Arabidopsis* roots

Cristina Ruberti ^{1,†} Elias Feitosa-Araujo ¹ Zhaolong Xu ^{2,3} Stephan Wagner ^{1,4,‡}
Matteo Grenzi ² Essam Darwish ^{5,6} Sophie Lichtenauer ¹ Philippe Fuchs ^{1,4,§}
Ambra Selene Parmagnani ² Daria Balcerowicz ⁷ Sébastien Schoenaers ⁷
Carolina de la Torre ⁸ Khansa Mekkaoui ⁹ Adriano Nunes-Nesi ¹⁰ Markus Wirtz ¹¹
Kris Vissenberg ^{7,12} Olivier Van Aken ⁵ Bettina Hause ⁹ Alex Costa ^{2,13,*}
and Markus Schwarzländer ^{1,*}

- 1 Institute of Plant Biology and Biotechnology, University of Münster, Münster, D-48143, Germany
- 2 Department of Biosciences, University of Milano, Milan, I-20133, Italy
- 3 Jiangsu Provincial Key Laboratory of Agrobiotechnology, Institute of Germplasm Resources and Biotechnology, Jiangsu Academy of Agricultural Sciences, Nanjing, Jiangsu 210014, China
- 4 Institute of Crop Science and Resource Conservation (INRES), University of Bonn, Bonn, D-53113, Germany
- 5 Department of Biology, Lund University, Lund, 22362, Sweden
- 6 Agricultural Botany Department, Faculty of Agriculture, Plant Physiology Section, Cairo University, Giza, 12613, Egypt
- 7 Integrated Molecular Plant Physiology Research, University of Antwerp, Antwerp, B-2020, Belgium
- 8 NGS Core Facility, Medical Faculty Mannheim, University of Heidelberg, Mannheim, D-68167, Germany
- 9 Department of Cell and Metabolic Biology, Leibniz Institute of Plant Biochemistry (IPB), Halle (Saale), D-06120, Germany
- 10 Departamento de Biologia Vegetal, Universidade Federal de Viçosa, Viçosa, 36570-900, Brazil
- 11 Centre for Organismal Studies (COS) Heidelberg, University of Heidelberg, Heidelberg, D-69120, Germany
- 12 Department of Agriculture, Plant Biochemistry and Biotechnology Lab, Hellenic Mediterranean University, Heraklion, 71410, Greece
- 13 Institute of Biophysics, Consiglio Nazionale delle Ricerche (CNR), Milan, I-20133, Italy

*Authors for correspondence: alex.costa@unimi.it (A.C.); markus.schwarzlander@uni-muenster.de (M.S.)

[†]Present address: Department of Biosciences, University of Milano, Milan, I-20133, Italy.

[‡]Present address: Max-Planck-Institute for Plant Breeding Research, Cologne, D-50829, Germany.

[§]Present address: Andermatt Biocontrol AG, Gossdrietwil, CH-6146, Switzerland.

C.R., S.W., A.C., and M.S. conceived the project and with specific input from M.W., A.N.N., K.V., O.V.A., and B.H. C.R., E.F.A., S.W., S.L., B.H., A.C., and M.S. designed the experiments. C.R., E.F.A., Z.X., S.W., M.G., E.D., S.L., P.F., A.S.P., D.B., S.S., C.D.T., K.M., O.V.A., and B.H. performed and analyzed the experiments. C.R., A.C., and M.S. wrote the manuscript with input from all co-authors. M.S. agrees to serve as the author responsible for contact and ensures communication.

The authors responsible for distribution of materials integral to the findings presented in this article in accordance with the policy described in the Instructions for Authors (<https://academic.oup.com/plcell>) are: Alex Costa (alex.costa@unimi.it) and Markus Schwarzländer (markus.schwarzlander@uni-muenster.de).

Abstract

Ca^{2+} signaling is central to plant development and acclimation. While Ca^{2+} -responsive proteins have been investigated intensively in plants, only a few Ca^{2+} -permeable channels have been identified, and our understanding of how intracellular Ca^{2+} fluxes is facilitated remains limited. *Arabidopsis thaliana* homologs of the mammalian channel-forming mitochondrial calcium uniporter (MCU) protein showed Ca^{2+} transport activity in vitro. Yet, the evolutionary complexity of MCU proteins, as well as reports about alternative systems and unperturbed mitochondrial Ca^{2+} uptake in knockout lines of MCU genes, leave critical questions about the in vivo functions of the MCU protein family in plants unanswered. Here, we

demonstrate that MCU proteins mediate mitochondrial Ca²⁺ transport in planta and that this mechanism is the major route for fast Ca²⁺ uptake. Guided by the subcellular localization, expression, and conservation of MCU proteins, we generated an *mcu* triple knockout line. Using Ca²⁺ imaging in living root tips and the stimulation of Ca²⁺ transients of different amplitudes, we demonstrated that mitochondrial Ca²⁺ uptake became limiting in the triple mutant. The drastic cell physiological phenotype of impaired subcellular Ca²⁺ transport coincided with deregulated jasmonic acid-related signaling and thigmomorphogenesis. Our findings establish MCUs as a major mitochondrial Ca²⁺ entry route in planta and link mitochondrial Ca²⁺ transport with phytohormone signaling.

Introduction

A characteristic of plant life is the ability to respond to environmental and developmental stimuli via flexible adjustments of metabolism, cell physiology, and the body plan. A signaling strategy that underpins a remarkable number of different responses is the modulation of intracellular free Ca²⁺ concentration (White and Broadley, 2003; McAinsh and Pittman, 2009; Kudla et al., 2018). Ca²⁺ signaling mediates responses to abiotic stress factors, such as heat, cold, salt stress, low oxygen, biotic interactions such as pathogen attack and symbiosis, and developmental stimuli to drive processes such as pollen tube and root hair growth. The precise modulation of the timing and cellular location of Ca²⁺ transients, as well as the physical association of different Ca²⁺ responder proteins with specific interactors, offer a large combinatorial landscape that enables highly specific responses in gene expression, physiology, and metabolism (Carafoli and Krebs, 2016; Edel et al., 2017; Elíes et al., 2020). While several of the many plant Ca²⁺ sensors and responders of the calmodulin (CaM), CaM-like, calcineurin-B-like (CBL), CBL-interacting protein kinase (CIPK), Ca²⁺-dependent protein kinase (CDPK/CPK), and Ca²⁺/CaM-dependent protein kinase families have been studied down to the molecular details (recently reviewed by Kudla et al., 2018), only a few Ca²⁺ channel proteins that mediate the Ca²⁺ transients in the first place are currently known (Hedrich, 2012; Kong et al., 2020). Prominent examples include the cyclic nucleotide-gated channels (Charpentier et al., 2016; Leitão et al., 2019; Meena et al., 2019; Tian et al., 2019), glutamate receptor-like channels (Toyota et al., 2018; Wudick et al., 2018; Nguyen et al., 2018a), reduced hyperosmolarity-induced Ca²⁺ increase channels (OSCA) (Hou et al., 2014; Yuan et al., 2014; Murthy et al., 2018; Thor et al., 2020), and Mid1-complementing activity, representing transmembrane proteins with potential for mechanosensing Ca²⁺ channel activity (Nakagawa et al., 2007; Yamanaka et al., 2010; Yoshimura et al., 2021).

While studies of Ca²⁺ signaling in plants have mainly focused on processes at the plasma membrane and in the cytosol and nucleus, it has been clear from early on that central processes of cellular Ca²⁺ regulation occur at and in organelles, including the vacuole, endoplasmic reticulum, peroxisomes, chloroplasts, and mitochondria (reviewed in Stael et al., 2012; Resentini et al., 2021b), where Ca²⁺-dependent proteins regulate key organelle functions (e.g. Weinl

et al., 2008; Jin et al., 2009). Some of the earliest evidence for intracellular Ca²⁺ transport in both plants and animals originates from Ca²⁺ uptake experiments with isolated mitochondria (DeLuca and Engstrom, 1961; Vasington and Murphy, 1962; Hodges and Hanson, 1965). Based on these studies, mitochondria had initially been postulated to act as major cellular Ca²⁺ stores. Subsequent in vivo Ca²⁺ measurements using aequorin in the mitochondria of *Arabidopsis thaliana* rosettes found that free Ca²⁺ concentrations were only slightly higher in the matrix than in the cytosol and that mitochondrial Ca²⁺ transients follow cytosolic Ca²⁺ transients, albeit with different signatures (Logan and Knight, 2003). These observations suggested that the operation of a transport system at the mitochondrial membranes modulates uptake and generates specific mitochondrial Ca²⁺ signatures (Logan and Knight, 2003; Loro et al., 2012).

Several Ca²⁺ uptake pathways have been described for animal mitochondria (Sparagna et al., 1995; Buntinas et al., 2001; Bondarenko et al., 2013), but the Ca²⁺ uniporter pathway was established as a major mode of Ca²⁺ entry, and its pharmacological and electrophysiological properties were described in detail (Kirichok et al., 2004; Hajnóczky and Csordás, 2010). In contrast, the Ca²⁺ fluxes measured in isolated plant mitochondria showed very different properties with respect to their pharmacology, the rates of uptake, and the requirement of phosphate, which is why the existence of a plant mitochondrial Ca²⁺ uniporter had been debated (Dieter and Marmé, 1980; Zottini and Zannoni, 1993), albeit in the absence of in vivo data. When the physical identities of the first components of the mitochondrial Ca²⁺ uniporter complex were elucidated in animals, that is, mitochondrial Ca²⁺ uniporter (MCU) and mitochondrial Ca²⁺ uptake (MICU) (Perocchi et al., 2010; Baughman et al., 2011; De Stefani et al., 2011), homologous genes were found also in plant genomes (Bick et al., 2012; Stael et al., 2012). Despite the conservation at the genetic level, noticeable differences became apparent, mirroring the functional differences observed earlier. For instance, multiple MCU copies exist in vascular plants, and a dominant-negative MCU paralog (MCUb; Raffaello et al., 2013) is lacking (Teardo et al., 2017). Similarly, the essential MCU regulator (EMRE), a component of the mitochondrial Ca²⁺ uniporter complex in metazoans and some fungi required for its function (Pittis et al., 2020), is absent in plant genomes (Sancak et al., 2013; Wagner et al., 2016; Wang et al., 2019). Instead of three genes

encoding isoforms of the regulatory Ca^{2+} -binding EF-hand protein MICU in mammals, Arabidopsis only contains a single MICU locus (Stael et al., 2012; Wagner et al., 2015; 2016). A functional investigation of Arabidopsis MICU showed that this protein has Ca^{2+} -binding activity and localizes to the mitochondrial inner membrane (Wagner et al., 2015). Arabidopsis *micu* knockout lines displayed deregulated mitochondrial Ca^{2+} signatures due to elevated concentrations of free matrix Ca^{2+} and enhanced uptake rates in planta, providing evidence for an inhibitory function of uniporter activity (Wagner et al., 2015).

Arabidopsis MCU1 and MCU2 localize to mitochondria (Teardo et al., 2017; Selles et al., 2018), while an additional localization to chloroplasts was reported for MCU6 in mesophyll cells (MCU6 was therefore referred to as chloroplast MCU [cMCU]) (Teardo et al., 2019). Arabidopsis MCU proteins were reported to show Ca^{2+} transport activity based on in vitro and heterologous analysis systems, that is, in planar lipid bilayers for MCU1 and MCU6 (Teardo et al., 2017, 2019), in human embryonic kidney 293 cells for MCU2 (Tsai et al., 2016), in yeast (*Saccharomyces cerevisiae*) for MCU1 and MCU2 (Selles et al., 2018), and in *Escherichia coli* for MCU6 (Teardo et al., 2019). These studies revealed that plant MCUs are sufficient for the formation of active channels, and there is no strict requirement for additional proteins, like for EMRE in metazoans. This is a feature that appears to be shared between plant MCUs and the MCUs of protozoa (Kovács-Bogdán et al., 2014; Chiurillo et al., 2017).

However, the critical question of whether MCUs are necessary for mitochondrial Ca^{2+} uptake in planta has remained unanswered, despite considerable efforts. As a consequence, the quantitative contribution of this putative Ca^{2+} uptake pathway relative to other potential routes of plant mitochondrial Ca^{2+} uptake (e.g. Carraretto et al., 2016a; reviewed in Wagner et al., 2016) also remains unclear. Furthermore, the physiological significance of MCU-mediated Ca^{2+} transport for other functions in plants has not been addressed in detail. Even though changes in the mitochondrial Ca^{2+} transient signature were observed in an Arabidopsis *mcu1* knockout background, those effects were subtle, and any direct indicator of mitochondrial Ca^{2+} uptake rate remained unchanged (Teardo et al., 2017), suggesting either a lack of a prominent role of MCU1 in mitochondrial Ca^{2+} uptake in vivo or functional backup by the remaining mitochondrial MCU isoforms. For *mcu2* knockout lines a fertility phenotype with reduced paternal transmission was observed and linked to defects in pollen tube germination and growth in vitro, which were, however, not evident in vivo (Selles et al., 2018). Whether the lack of MCU2 has an impact on mitochondrial Ca^{2+} transport in pollen or any other living tissue has remained unclear. The involvement of MCU6/cMCU in mediating in vivo Ca^{2+} flux into the chloroplast stroma has been reported, and phenotypes of Arabidopsis *mcu6* lines were linked to deregulation in chloroplast Ca^{2+} dynamics (Teardo et al., 2019).

Here, we addressed the in vivo function of the plant MCU family. We used a reverse genetic approach to generate an Arabidopsis triple MCU knockout line of *MCU1*, *MCU2*, and *MCU3* to overcome redundancy among MCU family members guided by Ca^{2+} imaging in root tips and the assessment of organismal phenotypes. Our findings indicate that MCU proteins mediate mitochondrial Ca^{2+} transport in planta and that this mechanism is the major route for rapid Ca^{2+} uptake.

Results

The properties of the MCU family in Arabidopsis suggest functional redundancy

We used Arabidopsis as a model to investigate the characteristics of the plant MCU family. MCU gene homologs are present across the plant kingdom and comprise small families in land plants (Teardo et al., 2017). A family of six Arabidopsis MCU homologs can be subdivided into two clades based on amino acid sequence identity: clade A (*AtMCU1* [At1g09575], *AtMCU2* [At1g57610]) and clade B (*AtMCU3* [At2g23790], *AtMCU4* [At4g36820], *AtMCU5* [At5g42610], *AtMCU6* [At5g66650]) (Figure 1, A and B; Supplemental File S1; Supplemental Data Set 1). All homologs share a predicted arrangement of an N-terminal signal peptide sequence and a loop containing a DVME amino acid motif, similar to the DIME motif found in the pore region of the mammalian MCU (Lee et al., 2015; Fan et al., 2020), flanked by two transmembrane helices (Supplemental Figure S1).

Based on sequence conservation and the observation that in vivo mitochondrial Ca^{2+} uptake was maintained in the absence of *MCU1* (Teardo et al., 2017), we reasoned that MCU family members might be functionally redundant in mitochondria. To test this hypothesis and to generate a model system that overcomes this redundancy (Figure 1M), we first combined two Arabidopsis T-DNA lines by crossing, giving rise to the clade A null mutant *mcu1 mcu 2* (abbreviated *mcu1 2*). The absence of *MCU1* and *MCU2* expression, respectively, was previously established for both parental lines (Teardo et al., 2017; Selles et al., 2018) and was confirmed for the individual homozygous lines (Supplemental Figure S2, B–D) and for *mcu1 2* (see paragraph below about Figure 3A). *MCU1* and *MCU2* were prioritized because they have diverged the least from the mammalian MCUs (Figure 1A), prior experimental evidence exists for their mitochondrial localization (Teardo et al., 2017; Selles et al., 2018), and their presence in the mitochondrial proteome has been experimentally confirmed (Wagner et al., 2015; Senkler et al., 2017; Fuchs et al., 2020). We further validated that both *MCU1* and *MCU2* are expressed in shoot and root tissues of 14-day-old wild-type seedlings (Figure 1C).

Mitochondrial Ca^{2+} dynamics remain unperturbed in *mcu1 2* roots at modest Ca^{2+} fluxes

To investigate whether mitochondrial Ca^{2+} dynamics were altered by MCU ablation in planta, we introduced the

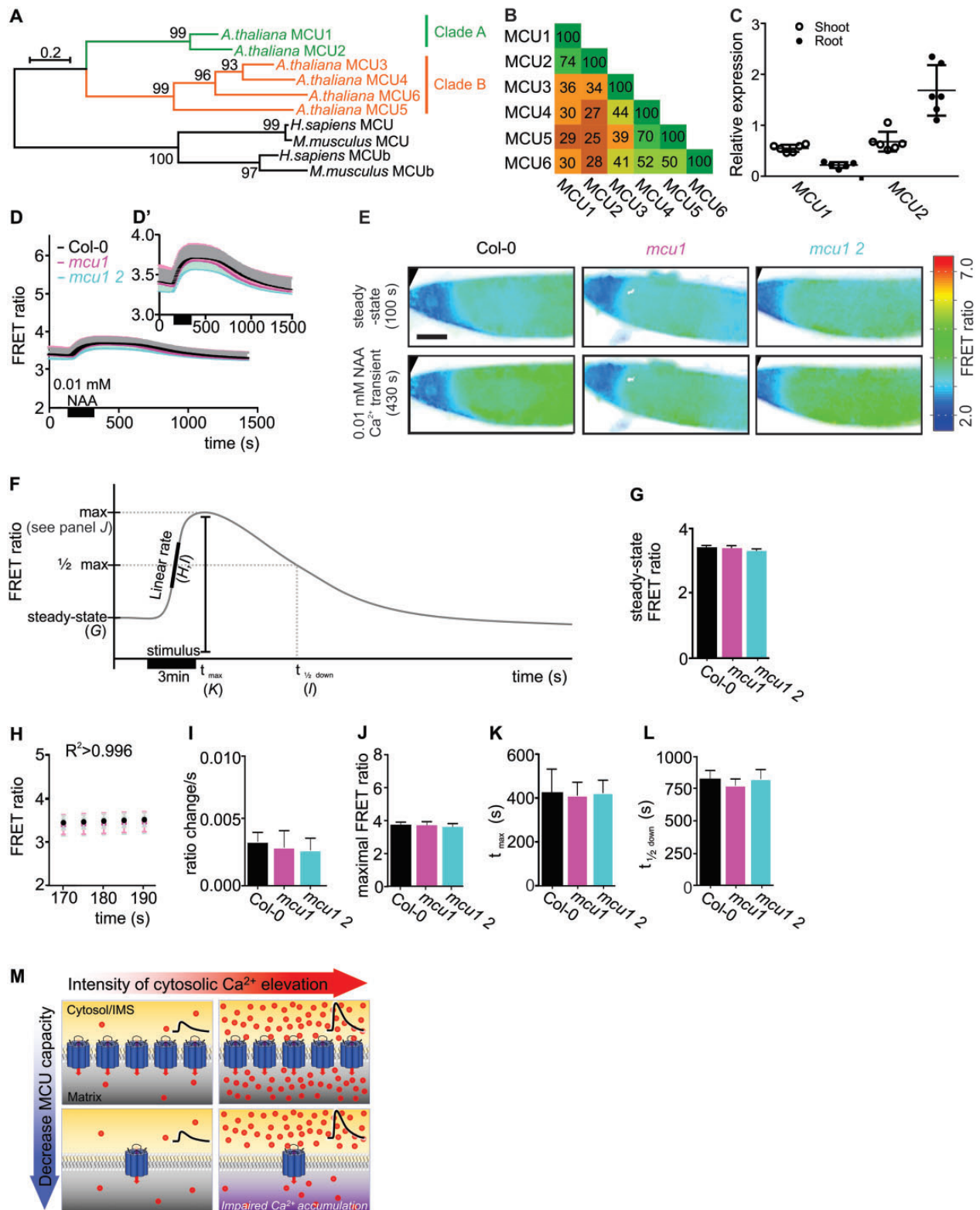


Figure 1 Mitochondrial matrix Ca^{2+} transients in response to stimulation with the auxin 1-naphthaleneacetic acid (NAA) in living root tips of *mcu1*, *mcu1 2*, and wild-type (Col-0) seedlings. **A**, Phylogenetic tree of *A. thaliana* and *M. musculus* proteins with homology to human MCU and MCUB. Scale bar corresponds to a distance of 0.20 amino acid substitutions per site. Bootstrap values, as calculated using 1,000 replicates, are indicated at the nodes. Color code indicates clustering of corresponding groups. Amino acid sequences from GenBank. *A. thaliana* MCU1 (NP_001322910.1), *A. thaliana* MCU2 (NP_001077733.1), *A. thaliana* MCU3 (NP_179959.1), *A. thaliana* MCU4 (NP_195400.2), *A. thaliana* MCU5 (NP_199075.1), *A. thaliana* MCU6 (NP_201466.1), *H. sapiens* MCU (NP_612366.1), *M. musculus* MCU (NP_001028431.2), *H. sapiens* MCUB (NP_060388.2), and *M. musculus* MCUB (NP_080055.2). **B**, Amino acid sequence identity of MCU homologs in *A. thaliana*. Identity percentage, as

(continued)

genetically encoded ratiometric Ca^{2+} sensor Yellow Cameleon 3.6 targeted to the mitochondrial matrix (4mt-YC3.6; Loro et al., 2012) into the *mcu1 2* background (Supplemental Figure S3). YC3.6 was selected over Aequorin to allow imaging at high spatial resolution and over other genetically encoded fluorescent Ca^{2+} sensors based on its ratiometric nature and its pH stability; YC3.6 has proven to be reliable for direct comparisons of resting Ca^{2+} levels between different genetic backgrounds, as well as for monitoring Ca^{2+} dynamics in the plant mitochondrial matrix where pH can vary significantly (Schwarzländer et al., 2012; Wagner et al., 2015; Behera et al., 2018; Grenzi et al., 2021). Furthermore, we recently established the linear rate increase in YC3.6 Förster resonance energy transfer (FRET) ratio towards the start of a Ca^{2+} transient as a particularly direct measure of in vivo Ca^{2+} uptake activity (as opposed to other key characteristics of the transient, which may be affected more strongly by indirect/secondary factors, such as Ca^{2+} buffering or clearance) (Wagner et al., 2015). To assess mitochondrial Ca^{2+} dynamics, we focused on root tips as a model and hotspot of intracellular Ca^{2+} dynamics. We compared *mcu1 2* to wild-type Col-0 seedlings, and we also included the *mcu1* single mutant for which previous work could not resolve any changes in mitochondrial Ca^{2+} uptake rate in vivo (Teardo et al., 2017). We evoked Ca^{2+} transients by applying the synthetic auxin 1-naphthalene acetic acid (NAA, 0.01 mM) in a custom perfusion setup for in vivo fluorescence microscopy (Figure 1, D and E; Supplemental Movie S1), a system that we previously optimized to study subcellular Ca^{2+} transport in Arabidopsis mutants (Wagner et al., 2015; Behera et al., 2018). We quantitatively assessed the following key characteristics of the transient, which hold key information about the properties of mitochondrial Ca^{2+} management (Figure 1F): the steady-state FRET ratio (Figure 1G), which provides an integrated measure of Ca^{2+} uptake, export and buffering in the matrix at baseline; the linear rate of the FRET increase in the starting phase of the Ca^{2+} transient (Figure 1, H and I), which

represents the most direct measure of in vivo Ca^{2+} uptake rate; the maximal FRET ratio (Figure 1J) as a measure of the maximal free Ca^{2+} accumulation reached at the peak of the transient (i.e. when uptake and clearance reach equal rates); the time that passes from the start of the transient to the maximum (t_{max} ; Figure 1K); and the time that passes after the peak to return to 50% of the amplitude ($t_{1/2 \text{ down}}$; Figure 1L) as an indicator of Ca^{2+} clearance efficiency, which may be modulated in response to primary changes in matrix Ca^{2+} accumulation. Before the NAA treatment (time 0–145 s), baseline matrix free Ca^{2+} levels were indistinguishable between lines (Figure 1, D, E, and G). Also, after the start of NAA perfusion, the characteristics of the mitochondrial Ca^{2+} transients did not differ between the three lines in any of their key properties (Figure 1, H–L). The absence of any differences between the lines indicates that, despite the lack of MCU1 and MCU2, NAA-induced mitochondrial Ca^{2+} uptake remained unaffected, and the mitochondrial uptake capacity was not limiting in any of the lines investigated.

Absence of MCU1 and MCU2 limits mitochondrial Ca^{2+} uptake at high Ca^{2+} fluxes

We next hypothesized that the mitochondrial Ca^{2+} uptake machinery becomes limiting only at sufficiently high in vivo Ca^{2+} flux (Figure 1M). To reveal putative differences in Ca^{2+} transport capacity, we aimed to drive Ca^{2+} transport activity, that is, the actual Ca^{2+} flux across the mitochondrial inner membrane, closer to the capacity limit of the uptake machinery. For this purpose, we used extracellular ATP (eATP) treatments at 0.01, 0.1, and 2.0 mM as a model stimulus to trigger mitochondrial Ca^{2+} transients in a dose-dependent manner ranging from low to high Ca^{2+} fluxes (Loro et al., 2012; Wagner et al., 2015; Matthus et al., 2019). Exposure to eATP triggered matrix Ca^{2+} transients in the root tips of all lines, and the elicited transients increased proportionally with increasing eATP concentration (Figure 2, A, H, and O). To achieve a systematic and quantitative

Figure 1 (Continued)

calculated using the Basic Local Alignment Search Tool (BLAST), is displayed by numerical values and color code (green, high identity; orange, low identity). C, Reverse transcription–quantitative PCR (RT–qPCR) analysis of *MCU1* and *MCU2* mRNA abundance in shoots and roots of 14-day-old Col-0 seedlings. Gene expression was normalized to SAND family protein expression for each sample. Error bars = sd, $n = 5–6$. D, FRET ratios over time in root tips of *mcu1*, *mcu1 2*, and Col-0 seedlings expressing the mitochondrial Ca^{2+} biosensor YC3.6, acquired under continuous perfusion and treated with 0.01 mM NAA for 3 min, as indicated by the black box on the x-axis. Whole frames as illustrated in part E were used for the quantification. D', same as (D) but y-axis scale and range adjusted. E, False-color images illustrating FRET ratios in root tips of seedlings expressing the mitochondrial YC3.6 in the indicated genetic backgrounds imaged under continuous perfusion shown at steady-state at 100 s (upper images) and during the Ca^{2+} transient induced by treatment with 0.01 mM NAA for 3 min at 430 s (lower images). A representative set of replicates of a complete time-series each is shown in Supplemental Movie 1. To compose the panel, images were cropped and image margins, when depicted, are colored in black. Low FRET ratios indicating low Ca^{2+} are shown in blue, and high FRET ratios indicating high Ca^{2+} are shown in red. Scale bar = 50 μm . F, Schematic representation of the extracted kinetic parameters of the sensor response depicted as letters in parenthesis and shown in parts (G)–(L). G, Steady-state FRET ratios before stimulus application in Col-0, *mcu1*, and *mcu1 2*. H, FRET ratio increase following 0.01 mM NAA application; linear region was selected by maximal goodness-of-fit measure of linear regression (R^2) for Col-0. I, Linear rate representing the slope of regression of part (H). J, Maximal peak FRET ratio after 0.01 mM NAA application. K, Time required to reach maximal FRET ratio after stimulus application. L, Time required to pass half-maximal ratio amplitude during recovery after the stimulus. $n \geq 9$; error bars = sd. No significant differences between Col-0 and the mutant lines were observed (One-way ANOVA with Dunnett's multiple comparisons test). M, Experimental rationale based on the hypothesis that MCU capacity for Ca^{2+} transport exceeds in vivo Ca^{2+} uptake activity from the cytosol/intermembrane space into the mitochondrial matrix. Hence, revealing in vivo MCU function requires the Ca^{2+} transport capacity to be limited below the required activity by knocking out a critical number of MCU genes.

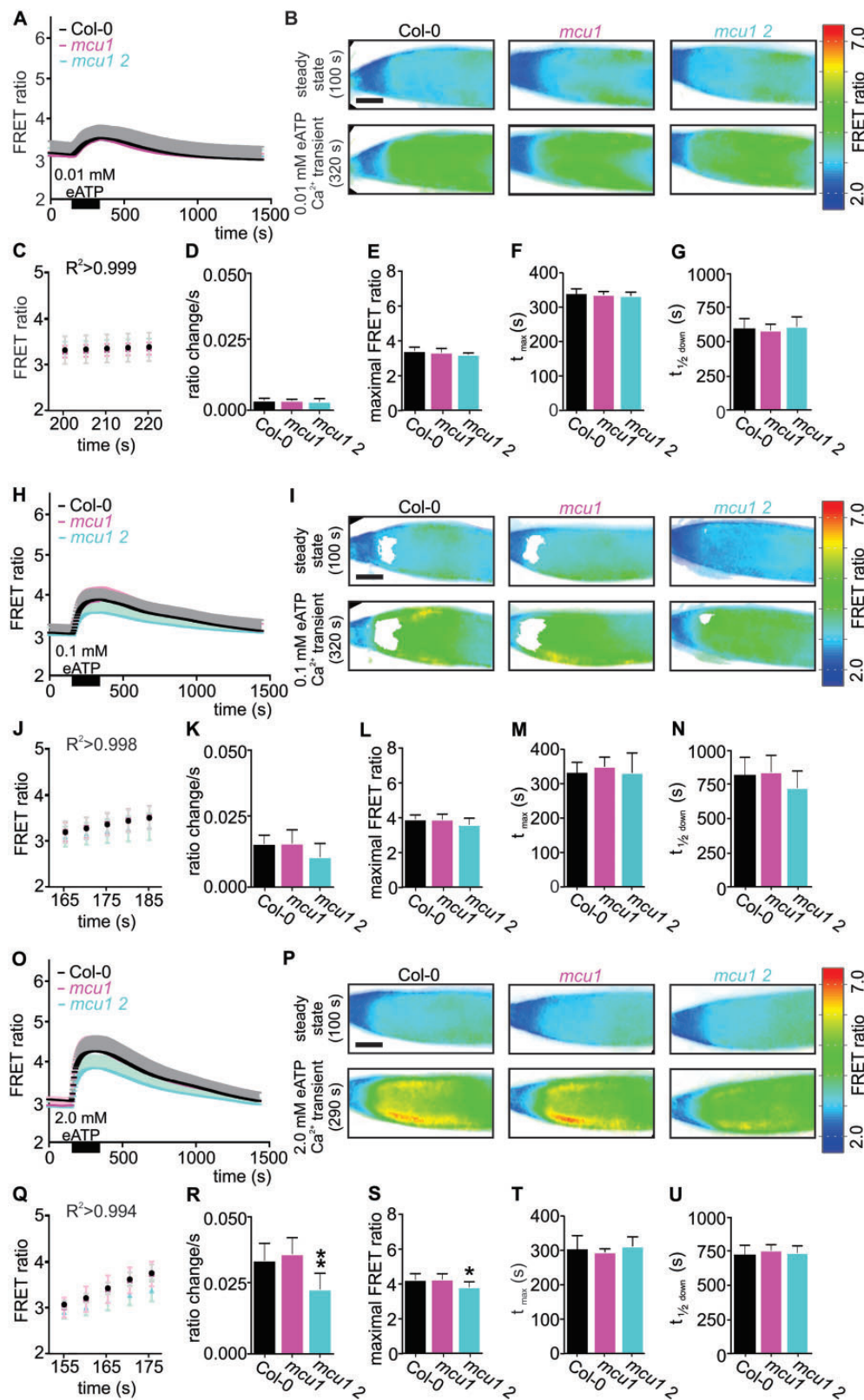


Figure 2 Genetic ablation of both *MCU1* and *MCU2* alters mitochondrial matrix Ca^{2+} transients induced by stimulation with eATP. A, FRET ratios over time in root tips of *mcu1*, *mcu1 2* and Col-0 seedlings expressing the mitochondrial YC3.6, acquired under continuous perfusion and treated with 0.01 mM eATP for 3 min. Whole frames as illustrated in (B) were used for the quantification. B, Ratiometric images illustrate FRET ratios in root tips of seedlings expressing 4mt-YC3.6 in the indicated genetic backgrounds acquired under continuous perfusion and shown at steady-state at 100 s (upper images) and during the Ca^{2+} transient induced by treatment with 0.01 mM eATP for 3 min at 320 s (lower images). A representative set of replicates of a complete time-series each is shown in [Supplemental Movie 2](#). To compose the panel, images were cropped and image

(continued)

comparison, we analyzed the individual characteristics of the eATP-induced transients as for NAA (Figures 1, D–L and 2). No difference between the lines was observed at 0.01 mM eATP (Figure 2, A–G; Supplemental Movie S2). At 0.1 mM eATP, the *mcu1 2* double null mutant showed a tendency toward lower rates of increases in matrix free Ca^{2+} levels, but this effect was not statistically significant (Figure 2, H–N; Supplemental Movie S3). At 2 mM eATP, however, the matrix Ca^{2+} transient was markedly different in the *mcu1 2* line (Figure 2, O–U; Supplemental Movie S4), which showed decreased rates of Ca^{2+} level elevation (Figure 2, Q and R) and lower maximal Ca^{2+} accumulation (Figure 2S). The time to reach the peak of the transient and the recovery remained unchanged (Figure 2, T and U).

These data show that mitochondrial Ca^{2+} uptake capacity became limiting in the *mcu1 2* line under high rates of cytosolic Ca^{2+} flux. Since such a limitation was not observed in the *mcu1* line, the limitation was due to either the combination of the two alleles or to *mcu2* alone. We decided against trying to pinpoint the specific quantitative in vivo contribution to the individual MCU loci since such an approach has proven futile in systems where total in vivo capacity exceeds the required in vivo activity (as is the case for most enzymes of central plant metabolism). Rather, we focused on further constraining total MCU capacity in order to investigate the significance of the MCU family. Since the mitochondrial Ca^{2+} uptake rate was reduced by approximately one-third in *mcu1 2* root tips (Figure 2R), there was considerable remaining capacity for mitochondrial Ca^{2+} uptake, which was mediated by either the remaining MCU homologs or by alternative transport systems.

The *mcu1 2 3* triple mutant shows a dramatic reduction in total MCU expression

To address the hypothesis that remaining genes from the MCU family provide functional backup in the *mcu1 2* background, we carefully selected an additional MCU locus to generate a triple knockout line. Only the clade A members MCU1 and MCU2 could be detected in mitochondrial proteomes (Wagner et al., 2015; Senkler et al., 2017; Fuchs et al., 2020). Yet, direct evidence for MCU3, MCU4, and MCU6 expression at the protein level comes from a recent mass spectrometry-based proteomic analysis of whole Arabidopsis tissues, in which only MCU5 was not found (Mergner et al., 2020). For a quantitative account of the relative expression of the MCU homologs, we measured their transcript abundance in roots and shoots by reverse transcription–

quantitative PCR (RT–qPCR). In roots, *MCU2*, *MCU3*, and *MCU4* were the most highly expressed MCU transcripts, with similar levels of abundance (Figure 3A), while *MCU3* was the most abundant MCU transcript in shoots (Supplemental Figure S4A). *MCU5* was below the detection limit in both roots and shoots. These data are in line with public mRNA-seq data (GENEVESTIGATOR, Hruz et al., 2008; Klepikova et al., 2016) (Supplemental File S2).

Based on the high *MCU3* transcript abundance in both roots and shoots, we selected *MCU3* to further limit total in vivo MCU capacity. Notably, *MCU3* shares the highest amino acid sequence identity with *MCU1* and *MCU2* relative to the other members of MCU clade B (Figure 1B) and exclusively localizes to the mitochondria, which we validated by subcellular localization analysis of an *MCU3*-GFP construct (Supplemental Figure S5). Therefore, we crossed an *mcu3* T-DNA insertion line into the *mcu1 2* background to generate *mcu1 mcu2 mcu3* (abbreviated *mcu1 2 3* hereafter; Supplemental Figure S6). RT–qPCR analysis of root and shoot tissue confirmed the absence of the *MCU1*, *MCU2*, and *MCU3* transcripts in the *mcu1 2 3* background (Figure 3A, Supplemental Figure S4A). The expression levels of *MCU5* and *MCU6* were similarly low in wild-type Col-0, *mcu1*, *mcu1 2*, and *mcu1 2 3*. Surprisingly, the abundance of the *MCU4* transcript decreased with increasing MCU ablation. Consequently, combined MCU transcript expression was reduced down to 22% in roots and 15% in shoots in the *mcu1 2 3* background (Figure 3A; Supplemental Figure S4A).

Tissue gradients of mitochondrial Ca^{2+} at baseline are perturbed in *mcu1 2 3* roots

To directly assess whether reduced MCU expression gives rise to changes in mitochondrial Ca^{2+} dynamics in *mcu1 2 3* seedlings, we introduced the mitochondrial Ca^{2+} biosensor 4mt-YC3.6 (Loro et al., 2012) into the triple mutant background. Exclusive mitochondrial localization of the sensor was confirmed by co-localization with MitoTracker (Supplemental Figure S7). Strikingly, we observed an apparent difference in the FRET ratio of the biosensor, indicating lower resting concentrations of matrix free Ca^{2+} in the root tips of *mcu1 2 3* seedlings (Figure 3B). While root tips of Col-0 showed a characteristic tissue gradient of matrix Ca^{2+} levels that increased from the root cap toward the elongation zone (see also Figures 1, E and 2, B, I, and P) (Wagner et al., 2015), this gradient was noticeably flattened in *mcu1 2 3*, but not in *mcu1* or *mcu1 2* (Figure 3B). To systematically

Figure 2 (Continued)

margins, when depicted, are colored in black. C, FRET ratio increase following 0.01 mM eATP application; linear region was selected by maximal goodness-of-fit measure of linear regression (R^2) for Col-0 ($R^2 > 0.998$ for *mcu1* and $R^2 > 0.992$ for *mcu1 2*) (D) Linear rate (ratio change per second) representing the slope of regression of (C). E, Maximal peak FRET ratio after 0.01 mM eATP application. F, Time required to reach maximal FRET ratio after stimulus application. G, Time required to pass half-maximal ratio during recovery after the stimulus. H–N, Analogous analysis for 0.1 mM eATP as in (A–G). Note that in (I), white image sectors within the root tissue region represent saturated pixels, which were removed from the ratiometric analysis. A representative set of replicates of a complete time-series each is shown in Supplemental Movie 3. O–U, Analogous analysis for 2.0 mM eATP as in (A–G). A representative set of replicates of a complete time-series each is shown in Supplemental Movie 4. Scale bars = 50 μm . $n \geq 6$; error bars = sd. * $P < 0.05$, ** $P < 0.01$ (One-way ANOVA with Dunnett's multiple comparisons test).

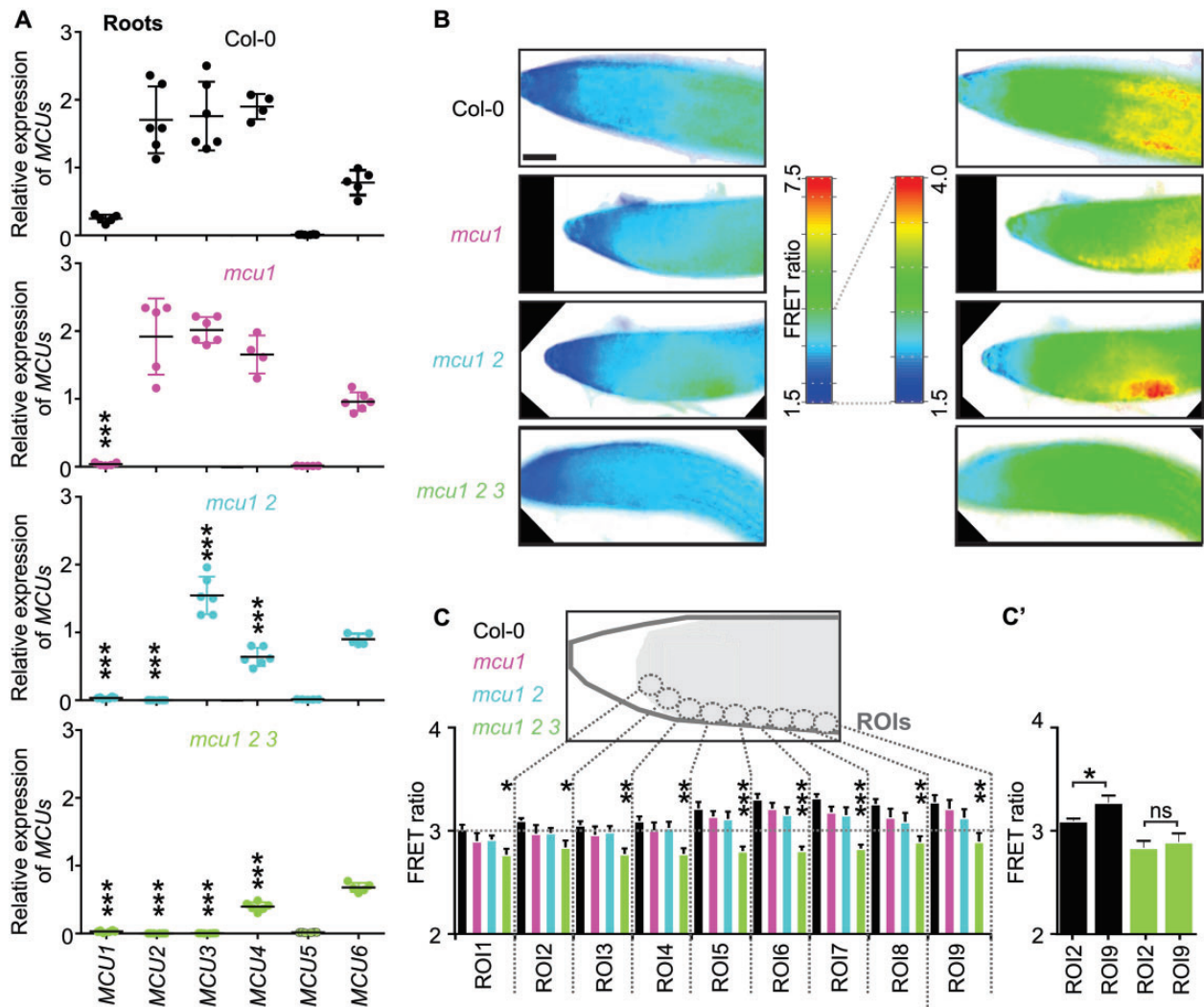


Figure 3 The baseline gradient of mitochondrial matrix Ca²⁺ concentration along the root tips of *mcu1*, *mcu1 2*, and wild-type is abolished in the *mcu1 2 3* genetic background. A, MCU expression in roots of 14-day-old seedlings in the indicated genetic backgrounds. The transcript abundance of each gene was quantified by RT-qPCR. Relative expression was calculated as the ratio between the transcript abundance of the gene studied and that of SAND family protein in the same sample. $n = 5-6$; error bars = sd. Asterisks indicate significant differences between each mutant and Col-0. *** $P < 0.001$ (One-way ANOVA with Dunnett's multiple comparisons test). B, Representative ratiometric false-color images of the steady-state FRET ratios along the root tips of seedlings expressing 4mt-YC3.6 in the wild-type (Col-0), *mcu1*, *mcu1 2*, and *mcu1 2 3* backgrounds. To compose the panel, images were cropped and image margins, when depicted, are colored in black. Left: FRET ratio color representation as in all other ratio images in this work (range from 1.5 to 7.5). Right: same images as on the right with adjusted FRET ratio color representation (range from 1.5 to 4.0), to enhance color resolution and clarify the differences that were systematically observed between *mcu1 2 3* and the other genetic backgrounds. Scale bar = 50 μm. C, Schematic representation of an Arabidopsis root tip depicting 9 ROIs with the same area (ROIs, dotted circles) along the longitudinal root axis into which the ratio images were subdivided for quantitative analysis of FRET ratios. In the chart, the resulting FRET ratio for each ROI is shown for wild-type (Col-0, black), *mcu1* (purple), *mcu1 2* (blue), *mcu1 2 3* (green). $n \geq 8$; error bars = sd. Asterisks indicate significant differences between each mutant line and Col-0 within each ROI: * $P < 0.05$; ** $P < 0.01$; *** $P < 0.001$ (One-way ANOVA with Dunnett's multiple comparisons test). C', Side-by-side comparison of steady-state FRET values of ROI2 with ROI9 in Col-0 and *mcu1 2 3*. ROI2 was used for the comparison rather than ROI1 to minimize the risk of including signal from the root cap. * $P < 0.01$; ns, not significantly different (Student's t test).

explore the effect of these tissue-specific changes, we analyzed the spatial distribution of FRET ratios by subdividing the sides of the root tip, where mitochondrial Ca²⁺ dynamics are particularly active (see Figures 1, E and 2, B, I, and P), into nine equally sized regions of interest (ROIs; Figure 3C). We excluded the root cap from the analysis, since it showed consistently low levels of mitochondrial free Ca²⁺ in all

genetic backgrounds, and it does not typically show any pronounced response to stimuli that trigger Ca²⁺ transients in the other tissues. In each of the nine ROIs, the matrix-free Ca²⁺ concentration was lower in *mcu1 2 3* roots compared to the wild-type control (Figure 3C), demonstrating that MCU activity is required to set basal matrix free Ca²⁺ concentrations in Arabidopsis. Furthermore, matrix Ca²⁺

levels progressively increased from ROI1 to ROI9 in Col-0 roots (Figure 3C), adding up to a marked difference, as quantified for ROI2 and ROI9 (Figure 3C'). This trend was maintained in *mcu1* and *mcu1 2* but was completely abolished in *mcu1 2 3* (Figure 3, C and C'). To control for general alterations in root tip architecture, we assessed the cellular organization in the root tips of *mcu1 2 3* and Col-0 (Supplemental Figure S4B). The overall root tip architecture was unchanged in *mcu1 2 3*, as indicated by the size and number of cell layers of the meristematic zone (Supplemental Figure S4, B–D) and the finding that *MCU1*, *2* and *3* were expressed in the cell types that are present in the ROIs (Supplemental Figure S4E), validating the ROI comparison between the different genetic backgrounds.

Mitochondrial Ca²⁺ uptake capacity is strongly impaired in *mcu1 2 3* root tissues

We next hypothesized that the shift in basal matrix free Ca²⁺ was due to the severe impairment of Ca²⁺ uptake in *mcu1 2 3*. To obtain direct in vivo information on the uptake, we monitored root tip Ca²⁺ transients triggered by 2.0 mM eATP in ROI2 and ROI9 (Figure 4; Supplemental Movie S5). Different signatures of the transients were observed between the different ROIs, with more pronounced transients of higher uptake rates and amplitude in ROI2 than in ROI9 (Figure 4, A, B, and H). Yet, in both ROIs, as well as all ROIs in between, the impairment of the transient (i.e. uptake rate and maximal FRET ratio) in *mcu1 2* was exacerbated in *mcu1 2 3* (Figure 4, C–E, I–K). In ROI9, the uptake rate was close to 0 in *mcu1 2 3*, and the transient was nearly completely abolished (compromising the accurate measurement of transient characteristics; Figure 4, I–M). In ROI2, a transient still occurred in *mcu1 2 3*, but the uptake rate was diminished to <25% that of Col-0 (Figure 4, B–D). Ca²⁺ clearance efficiency, as indicated by $t_{1/2 \text{ down}}$, was perturbed in ROI2 but not in ROI9 (Figure 4, G and M). Systematic analyses using a weaker dose of the eATP stimulus that triggered a weaker matrix Ca²⁺ transient (0.1 mM eATP) yielded similar results (Supplemental Figure S8). Only at the weakest transient (0.01 mM eATP) did the differences between the genotypes start to become obscured (Supplemental Figure S9).

The data not only demonstrate that MCU proteins mediate mitochondrial Ca²⁺ uptake in vivo but also that MCUs underpin the dominant mechanism for rapid matrix uptake in Arabidopsis root tips. The residual uptake activity in the *mcu1 2 3* line might have been due to the remaining MCUs or to alternative mechanisms, which will need to be resolved in the future. In either case, those activities clearly make only minor contributions to mitochondrial Ca²⁺ uptake capacity in the root tip and cannot compensate for the loss of *MCU1*, *MCU2*, and *MCU3* when cytosolic Ca²⁺ level elevations are rapid and pronounced. The altered mitochondrial Ca²⁺ dynamics of the *mcu1 2 3* line were independent of the model stimulus that evoked the primary cytosolic Ca²⁺ elevation, as validated by auxin application (0.01 mM NAA;

Supplemental Figure S10, A–F) to trigger a mild (non-limiting) Ca²⁺ response and an acute osmotic challenge via sequential administration and washout of 200 mM sorbitol to trigger a pronounced Ca²⁺ elevation at washout (Supplemental Figure S10, G–L; as optimized previously for guard cells and roots; Loro et al., 2012; Corso et al., 2018).

We tried to construct independent multi-knockout lines by clustered regularly interspaced short palindromic repeats and CRISPR-associated protein 9 (CRISPR–Cas9)-mediated genome editing but were not successful. Independent lines are typically required to test for the potential involvement of second site mutations and to validate the link between genetic locus and phenotype. In the specific system combining loci of one gene family, the link between the *MCU* loci and the mitochondrial Ca²⁺ transport phenotype is demonstrated by the exacerbation of the phenotype from *mcu1 2* to *mcu1 2 3*. It is highly unlikely that such a specific phenotype arises by chance, which rules out potential contributions by secondary site mutations with similarly high confidence as genetically independent lines. To validate this experimentally, we generated lines expressing *MCU2* cDNA (35S:*MCU2*) in either the *mcu1 2 3* background or the Col-0 wild-type background (Supplemental Figure S11, A and B). The *MCU2* transcript was detected at high abundance (Supplemental Figure S11C), allowing for two independent lines each to be used for in vivo Ca²⁺ analysis using 2 mM ATP as the stimulus (Supplemental Figure S12). Even though the lines analyzed were in the T2 generation, that is, segregating for the 35S:*MCU2* insertion locus, the mitochondrial Ca²⁺ dynamics in *mcu1 2 3 35S:MCU2* roots were rescued, as evident from the average uptake rates (Supplemental Figure S12), demonstrating that the impairment of MCU function was indeed causative for the observed phenotype in mitochondrial Ca²⁺ uptake. Interestingly, the roots of Col-0 35S:*MCU2* seedlings showed even higher uptake rates than the wild-type, as well as increased matrix resting levels, confirming the correlation between *MCU* abundance due to elevated *MCU* expression and Ca²⁺ uptake capacity. The finding that introducing *MCU2* alone led to a functional rescue adds evidence for functional redundancy among *MCU1*, *2* and *3*. Functional redundancy among the three *MCU* genes is further supported by the observation that mitochondrial Ca²⁺ uptake in the *mcu3* single mutant was similar to that of the wild-type (Supplemental Figure S12). This control shows that the combined absence of three *MCU* proteins, rather than *MCU3* alone, is responsible for the major impairment of Ca²⁺ uptake capacity in *mcu1 2 3* (as compared to *mcu1 2*, where the effect is much milder; Figure 4).

Cytosolic Ca²⁺ dynamics remain unperturbed in *mcu1 2 3* roots

We next hypothesized that diminished mitochondrial Ca²⁺ uptake would modify the primary Ca²⁺ transient in the cytosol. Cytosolic Ca²⁺ signatures are shaped by mitochondrial Ca²⁺ transport, which acts as a capacitor, and these

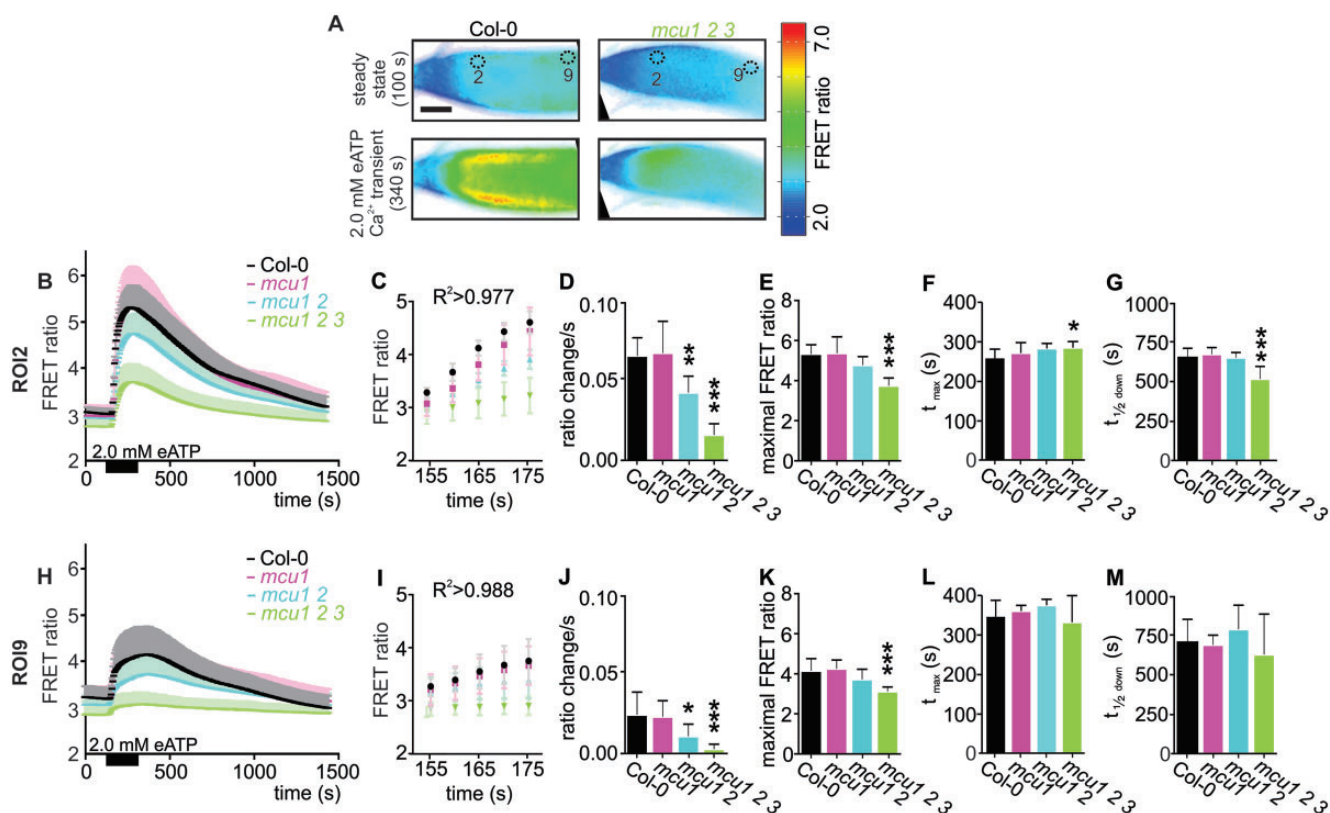


Figure 4 The mitochondrial matrix Ca^{2+} transient triggered by 2.0 mM eATP shows progressive impairment with progressive ablation of MCU isoforms. A, Representative ratiometric images illustrate FRET ratios in root tips of seedlings expressing 4mt-YC3.6 in wild-type (Col-0) and *mcu1 2 3* imaged under continuous perfusion and shown at steady-state before stimulus application at 100 s (upper images) and at 340 s (lower images) during the Ca^{2+} transient induced by treatment with 2.0 mM eATP for 3 min. A representative set of replicates of a complete time-series each is shown in [Supplemental Movie S5](#). To compose the panel, images were cropped and image margins, when depicted, are colored in black. ROI2 and ROI9, which are analyzed at detail in the other panels of this figure, are depicted by black dotted circles. Scale bar = 50 μm . B, FRET ratio dynamics of ROI2 in *mcu1*, *mcu1 2*, *mcu1 2 3*, and Col-0 seedlings expressing 4mt-YC3.6, acquired under continuous perfusion and treated with 2.0 mM eATP for 3 min. C, FRET ratio increase following 2.0 mM eATP application; linear region was selected by maximal goodness-of-fit measure of linear regression (R^2) for Col-0. D, Linear rate representing the slope of regression of (C). E, Maximal FRET ratio after 2.0 mM eATP application. F, Time required to reach maximal FRET ratio after stimulus application. G, Time required to pass half-maximal ratio during recovery after stimulus application. H–M, Analogous analysis for ROI9 as in (B–G). $n = 8$; error bars = SD. Asterisks indicate significant differences between each mutant line and Col-0: * $P < 0.05$; ** $P < 0.01$; *** $P < 0.001$ (One-way ANOVA with Dunnett’s multiple comparisons test).

signatures were shown to be modified by the impairment of the mitochondrial Ca^{2+} uniporter complex in mammalian cell systems (Drago et al., 2012; Logan et al., 2014; Rasmussen et al., 2015).

We expressed the NES-YC3.6 Ca^{2+} sensor in the cytosol (Krebs et al., 2012) in the *mcu1 2 3* background and monitored the resting state of cytosolic free Ca^{2+} , as well as Ca^{2+} transients elicited by 2.0 mM eATP (Figure 5A; Supplemental Movie S6). *mcu1 2 3* and Col-0 showed identical resting states of cytosolic free Ca^{2+} (Figure 5B), and no change was observed in any of the characteristics of the Ca^{2+} transient in ROI2 and ROI9 either (Figure 5, C–N). We also systematically analyzed ROI1 and ROI3 to ROI8 and did not detect any difference in the cytosolic Ca^{2+} transient (Supplemental Figure S13). These data strongly suggest that even severe impairment of Ca^{2+} uptake into the mitochondria (Figure 4, H–J) does not alter the Ca^{2+} transients in the cytosol of root tips (Figure 5, I–K). The contribution made

by the mitochondria may be sufficiently minor to be buffered or compensated for by other mechanisms. As a result, the impaired Ca^{2+} dynamics phenotype is highly specific to the mitochondrial matrix.

Impaired mitochondrial Ca^{2+} uptake in *mcu1 2 3* is not associated with changes in gross plant development under a broad spectrum of conditions

Despite the dramatic cell physiological phenotype of diminished matrix Ca^{2+} uptake in the *mcu1 2 3* line, the plants appeared to grow and develop normally. The systematic assessment of plant growth in soil, including quantifying rosette size (Supplemental Figure S14A), photosynthetic efficiency (Supplemental Figure S14B), and silique length (Deng et al., 2016) (Supplemental Figure S14C) did not reveal any apparent differences. The same was true for seedlings grown on agar plates, as assessed for leaf area and root length (Supplemental Figure S15). Also, the external

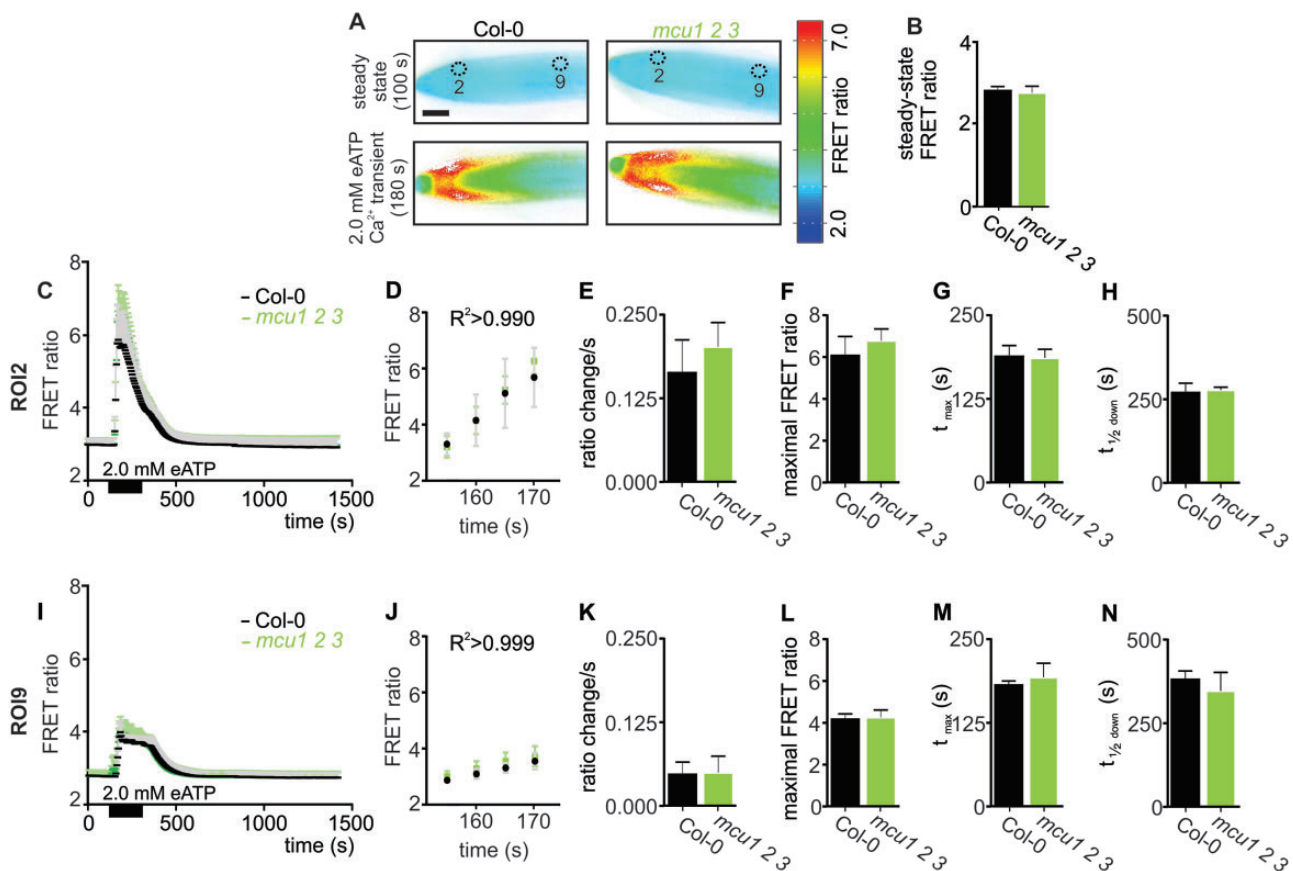


Figure 5 Cytosolic Ca^{2+} transients in root tips induced by treatment with eATP are unchanged in *mcu1 2 3*. A, Representative FRET images of Col-0 and *mcu1 2 3* root tips expressing the cytosolic Ca^{2+} sensor NES-YC3.6 imaged under continuous perfusion and shown at steady-state before stimulus application at 100 s (upper images) and at 180 s (lower images) during the Ca^{2+} transient induced by treatment with 2.0 mM eATP for 3 min. A representative set of replicates of a complete time-series each is shown in Supplemental Movie 6. Scale bar = 50 μm . B, Steady-state FRET ratios in the roots before the application of 2.0 mM eATP. C, FRET ratio dynamics of ROI2 of seedlings expressing NES-YC3.6 acquired under continuous perfusion and treated with 2.0 mM eATP for 3 min. D, FRET ratio increase following 2.0 mM eATP application; linear region was selected by maximal goodness-of-fit measure of linear regression (R^2) for Col-0. E, Linear rate representing the slope of regression of (D). F, Peak FRET ratio after 2.0 mM eATP application. G, Time required to reach maximal FRET ratio after stimulus application. H, Time required to pass half-maximal ratio amplitude during recovery. I–N, Analogous analysis for ROI9 as in (C)–(H). $n = 8$; error bars = sd. No significant differences between Col-0 and *mcu1 2 3* were observed (Student's *t* test).

challenge of seedlings with different cues to induce osmotic, ionic, hormonal, and redox stress did not lead to differential growth behavior (Supplemental Figure S16). Since mitochondrial function and Ca^{2+} dynamics have been shown to be critical for optimal tip growth, we specifically assessed tip-growing root hairs and pollen tubes for their developmental and growth properties (Supplemental Figure S17) (Schiefelbein et al., 1992; Monshausen et al., 2008; Zhang and Turner, 2008; Schoenaers et al., 2017). However, *mcu1 2 3* behaved like Col-0 for all of the tested parameters. The impairment of mitochondrial electron transport and the induction of retrograde signaling by the Complex III inhibitor antimycin A (Wagner et al., 2019; Fuchs et al., 2022) did not result in any growth responses in seedlings (Supplemental Figure S18). In addition, no differences were detected in recovery after submergence (in darkness or continued light-dark cycles) and hypoxia stress, which we employed due to their impact on mitochondrial respiratory function and cytosolic Ca^{2+} levels (Wagner et al., 2019; Igamberdiev and

Hill 2018) (Supplemental Figure S19). The characteristic gradual Ca^{2+} accumulation that occurs under hypoxia in the cytosol and the mitochondria of seedlings over several hours was unchanged (Supplemental Figure S19, D and E), indicating sufficient residual capacity for the low rates of mitochondrial Ca^{2+} transport involved. Whole plant darkening led to a small but significant difference in chlorophyll content between rosettes of Col-0 and the *mcu1 2 3* line after 11 days of treatment (Supplemental Figure S20).

mcu1 2 3 seedlings show deregulated jasmonic acid homeostasis and impaired touch signaling

To validate the absence of gross phenotypic consequences at a global gene expression scale or to pinpoint the impact of disrupted MCU capacity and matrix free Ca^{2+} dynamics, we performed a comparative transcriptome analysis of roots from hydroponically grown *mcu1 2 3* and Col-0 seedlings without additional stimulation. Five replicates of pooled seedling roots were analyzed each. The vast majority of

transcripts remained unchanged between the genotypes, confirming the absence of major pleiotropic rearrangements (Figure 6A). However, a specific set of 172 genes showed differential abundance (P -adjusted < 0.05; $-1.5 \leq$ fold change ≥ 1.5), the majority of which (159) were repressed in *mcu1 2 3* compared to Col-0 (Supplemental Data Sets 2 and 3 for the complete lists of transcripts). The ontologies of the differentially expressed genes pointed toward functions in the response to stress and to external stimuli (Figure 6B). At the center of the different categories was a remarkable enrichment of transcripts involved in jasmonic acid (JA) metabolism (Zhang and Turner, 2008).

To explore the connection between MCU function and the transcriptional regulation of JA metabolism, we compared the 172 differentially abundant transcripts in *mcu1 2 3* with the recently reported core set of 82 genes regulated by the JA-activated transcription factor MYC2 (i.e. the “MYC2 regulon” Van Moerkercke et al., 2019). Fourteen genes were shared in both datasets, representing a strong statistical enrichment, and all 14 transcripts were repressed in *mcu1 2 3* (Supplemental Figure S21A; Supplemental Data Set 4). To test the hypothesis of altered JA homeostasis, we selected a set of established JA-related transcripts involved in JA biosynthesis (LOX3, OPR3, and AOS (Mueller, 1997; Wasternack, 2007; Schaller and Stintzi, 2009; Beaugelin et al., 2019), JA catabolism (JAO2 and JAO4; Caarls et al., 2017; Smirnova et al., 2017), and JA-mediated signaling pathways (MYC2, JAZs, NPR3, WRKY53, and GRX480) (Huang et al., 2017; Ruan et al., 2019; Van Moerkercke et al., 2019) and assessed their expression in the *mcu1 2 3* root transcriptome, thus also including those transcripts that did not pass the criteria of P adjusted < 0.05 and $-1.5 \leq$ fold change ≥ 1.5 of the global analysis. All of these JA-related transcripts were repressed in *mcu1 2 3* (Figure 6C). We selected four of the JA-related transcripts (OPR3, MYC2, JAZ10, and JAO4), as well as two stress marker transcripts (CPK28 and WRKY40) that were significantly repressed in the *mcu1 2 3* transcriptome dataset for quantification by RT-qPCR in seedlings that were grown independently of the material used for the transcriptome analysis. All six transcripts were present at lower levels in *mcu1 2 3* versus Col-0 (Figure 6D; Supplemental Figure S21, B–D). An assessment of transcripts encoding Group VII ERF transcription factors, ethylene signaling components, and targets of mitochondrial retrograde regulation (De Clercq et al., 2013) did not reveal any concerted response (Supplemental Figure S21E).

To investigate whether the transcriptomic fingerprint reflected changes in the contents of JA signaling intermediates, we quantified 12-oxo-phytodienoic acid (OPDA), dinor-oxo-phytodienoic acid (dn-OPDA), JA, and jasmonoyl-L-isoleucine (JA-Ile) in the roots of hydroponically grown *mcu1 2 3* and Col-0 seedlings. JA and JA-Ile levels were doubled in the roots of *mcu1 2 3* compared to Col-0 roots (Figure 6E), which was unexpected considering the positive feedback control of JA biosynthesis. OPDA and dn-OPDA were also present at higher levels in the mutant, but that

change was variable between independent experimental repetitions (Figure 6E; Supplemental Figure S21D). To determine whether this inconsistent pattern was due to regulation at the protein level, we analyzed ALLENE OXIDASE CYCLASE (AOC) protein levels by immunoblotting (Stenzel et al., 2003). These levels were largely unchanged between the *mcu* backgrounds and the Col-0 control (Supplemental Figure S21G). Taken together, the transcriptome analysis and the analytical phytohormone measurements uncovered deregulated JA metabolism and signaling as well as stress responses in roots of the *mcu1 2 3* mutant, pointing to an unexpected link between mitochondrial Ca²⁺ dynamics and JA homeostasis.

Recent observations have suggested that the integrated effects of mitochondrial regulation, Ca²⁺, and JA are involved in touch responses and thigmomorphogenesis (Van Aken et al., 2016; Van Moerkercke et al., 2019; Xu et al., 2019; Darwish et al., 2022), prompting us to assess the responses of *mcu1 2 3* and Col-0 plants to a reoccurring touch stimulus (Darwish et al., 2022) (Figure 6, F–K). The resulting changes in rosette area, bolting time and inflorescence height consistently suggested an impaired thigmomorphogenesis response in the *mcu1 2 3* mutants. While the touch stimulation of the shoot has no direct equivalent in the root, we devised a method for analyzing the mechanoreponse of root growth using an agar penetration assay (Mousavi et al., 2021). No differences in root growth were observed between *mcu1 2 3* and the Col-0 control (Supplemental Figure S22). The discovery of a link between mitochondrial Ca²⁺ uptake, JA signaling and touch responses, as well as the potential deregulation of JA feedback control, opens the door for future work to resolve the connection in mechanistic detail and to unravel the impact of mitochondrial Ca²⁺ uptake capacity on processes linked to JA homeostasis and touch signaling.

Discussion

The major route of plant mitochondrial Ca²⁺ uptake is via MCU channels

Reverse genetics and in vivo Ca²⁺ imaging demonstrated that MCU proteins mediate Ca²⁺ uptake into the mitochondrial matrix in living Arabidopsis tissues. Exploiting the combinational ablation of three members of the MCU family and challenging these mutants with increasing intracellular Ca²⁺ fluxes, as elicited by NAA and eATP (Figures 1–4; Supplemental Figures S8 and S9), pinpointed the redundant functionality of MCU family proteins, which could be overcome by combining mutant lines. The additive Ca²⁺ uptake phenotype from *mcu1 2* to *mcu1 2 3* provides a clear demonstration that functional redundancy was overcome and that MCU capacity decreased beyond the normally required activity in vivo. These findings resolve the long-standing question of the function of a Ca²⁺ uniporter in plant mitochondria and unify the previous observations of (1) mitochondria-specific Ca²⁺ signatures in planta (Logan and Knight, 2003; Loro et al., 2012); (2) the activation of

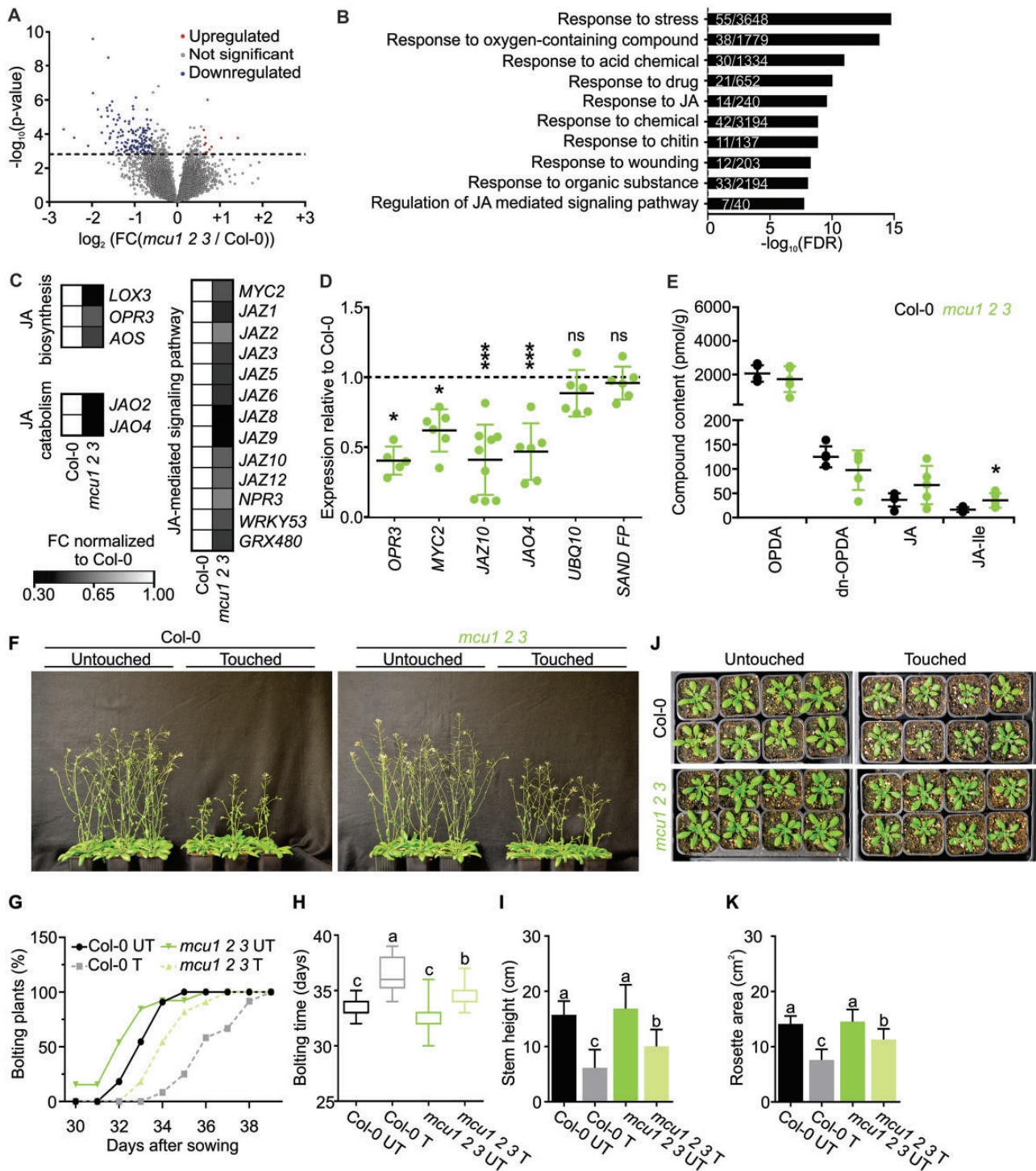


Figure 6 Deregulated jasmonic acid homeostasis and impaired thigmomorphogenesis response in *mcu1 2 3* seedlings. **A**, Volcano plot of the seedling root transcriptome of *mcu1 2 3* compared to Col-0. \log_2 fold change (FC, x-axis) is plotted against the $-\log_{10}$ P-value (y-axis). Downregulated transcripts (FC ≤ -1.5 and P -adjusted < 0.05): blue; upregulated transcripts (FC ≥ 1.5 and P -adjusted < 0.05): red; not differentially abundant transcripts: gray. **B**, Gene ontology (GO) enrichment analysis for transcripts that were down regulated in *mcu1 2 3*. The 10 categories with the highest enrichment are sorted by decreasing false discovery rate. Numerator: number of differentially abundant transcripts in the transcriptome dataset. Denominator: number of total genes curated for the GO term. **C**, Heat map of the relative abundance of JA-related transcripts from the transcriptome dataset shown in panel (A). FC values of *mcu1 2 3* normalized to Col-0 (set to 1). The color gradient from white to black represents values from 1.0 (expression like Col-0) to 0.30 (expression lower than Col-0). **D**, Expression of selected JA-related transcripts, and *UBQ10* and *SAND FP* for reference, as measured by RT-qPCR in roots of Col-0 and *mcu1 2 3* seedlings. Relative expression was calculated as the ratio between the abundance of the respective transcript and of the *UBIQUITIN-CONJUGATING ENZYME 21* (*UBC21*) reference transcript in the same sample. Relative expression is normalized to Col-0 (set to 1, black dotted line). $n = 5-6$; error bars = SD. * $P < 0.05$; *** $P < 0.001$ (Student's *t* test). **E**,

(continued)

mitochondrial Ca²⁺ uptake when an Arabidopsis homologue of the metazoan MCU regulator MICU is absent (Wagner et al., 2015); and (3) the ability of MCU1 and MCU2 to act as Ca²⁺ channels in vitro and in recombinant systems (Tsai et al., 2016; Teardo et al., 2017; Selles et al., 2018). The concomitant ablation of MCU isoforms 1, 2, and 3 (Figure 3A; Supplemental Figure S4A) diminished the in vivo Ca²⁺ uptake down to residual rates (Figure 4; Supplemental Figures S8 and S9) and clearly demonstrated the dominant role of MCU proteins in rapid mitochondrial Ca²⁺ uptake. Conversely, the 35S:MCU2 lines showed the opposite effect, that is, increased matrix free Ca²⁺ at baseline and increased Ca²⁺ uptake rates (Supplemental Figure S12), suggesting that (1) MCU expression and mitochondrial Ca²⁺ uptake capacity are directly linked and (2) even MCU abundance in the wild-type can be limiting for transport capacity. While the *mcu1 2 3* line established here may be considered a strong knockdown line of total MCU capacity specifically of the mitochondria, a full knockout line may be generated in the future to also abolish any remaining MCU capacity. MCU5 did not appear to be expressed under any condition studied so far, but MCU4 and/or MCU6 may indeed provide the remaining Ca²⁺ transport capacity observed here. However, including MCU6 in a higher-order knockout line would be complicated by the recent observation that MCU6 also localizes to chloroplasts (Teardo et al., 2019) (even though MCU6 expression in the plastid envelope exclusively in green tissue is surprising and deserves further investigation of the underlying regulation of protein targeting). A higher-order mutant line that includes MCU6 knockout could give rise to organismal effects that may arise from both the mitochondria and chloroplasts, complicating the mechanistic dissection of phenotypes. Hence, in addition to a sextuple *mcu1 2 3 4 5 6* line, the sextuple line complemented with plastid-specific MCU6 appears to be most suitable to remove any residual mitochondrial MCU capacity while ruling out primary effects beyond the mitochondria.

Reverse genetics of proteins with redundant functions cannot reveal the relative quantitative contributions of the individual proteins in the wild-type in a straightforward manner. This is particularly true for a system in which the overall in vivo capacity exceeds the required in vivo activity. The clade A proteins MCU1 and MCU2, but no clade B proteins, were detected by mitochondrial proteomics (Wagner et al., 2015; Senkler et al., 2017; Fuchs et al., 2020) and also showed a higher peptide coverage than clade B proteins in

tissue-specific proteomics (Mergner et al., 2020), suggesting that MCU1 and MCU2 are the most abundant MCU proteins in Arabidopsis mitochondria. Yet, the *mcu1 2 3* triple mutant showed a stronger impairment in mitochondrial Ca²⁺ uptake than the *mcu1 2* double mutant (Figures 3 and 4). This observation suggests that the absence of MCU1 and MCU2 (or MCU2 on its own), abolishes any excess uptake capacity, rendering the remaining uptake system limiting, which gives rise to a strong additional impairment of uptake rate in response to MCU3 ablation. Loss of MCU3 alone is not responsible for the strong impairment of matrix Ca²⁺ uptake in the *mcu1 2 3* background, since the *mcu3* line showed Ca²⁺ dynamics similar to those of the Col-0 control (Supplemental Figure S12). The idea that the three MCU proteins acts redundantly and that the MCU capacity is increasingly limited in higher-order mutants is supported by the finding that defects in Ca²⁺ uptake are dependent on the intensity of the stimulus and that the impairment of the Ca²⁺ uptake rate was already pronounced in *mcu1 2* root tips when exposed to 2 mM eATP (down to 65% of Col-0 in ROI2 and 44% of Col-0 in ROI9; Figure 4, D and J). It can be concluded that (1) MCU proteins provide the dominant path for Ca²⁺ to rapidly enter the mitochondria in root tips and (2) any remaining MCU4, MCU5, and MCU6 proteins combined provide at most a minor fraction of the total capacity for rapid mitochondrial Ca²⁺ uptake (24% in ROI2; 10% in ROI9; Figure 4, D and J). However, it was also evident that very slow rates of Ca²⁺ accumulation in the matrix, which were characteristic during hypoxia (Supplemental Figure S19, D and E), were not affected in *mcu1 2 3* seedlings. In that case, it appears that the remaining capacity is not limiting.

We cannot and do not aim to assess the relative quantitative contributions of the individual MCU loci to mitochondrial Ca²⁺ uptake capacity. Instead, we provide a system that offers different degrees of limited total MCU capacity in vivo. We focused our investigations on Arabidopsis root tips of young seedlings as a model system for highly standardized in vivo analyses, but it is possible that other tissues express alternative transporters. A direct impact on mitochondrial Ca²⁺ dynamics in green tissues was not systematically assessed here. Yet, circumstantial support for the functional importance of MCU1, MCU2, and MCU3 in the shoot comes from the finding that the transcript responses were similar in the roots and shoots of *mcu1 2 3* (Figure 6D; Supplemental Figure S21D). Future work will need to

Figure 6 (Continued)

Quantification of OPDA, dn-OPDA, JA, and JA-Ile in roots of Col-0 and *mcu1 2 3* seedlings. *n* = 5; error bars = SD. **P* < 0.05 (Student's *t* test). F, Representative images of Col-0 wild-type and *mcu1 2 3* plants with and without touch treatment (touched, untouched) applied for 4 weeks twice daily from 14 days after transfer to the growth room. G, Percentage of bolting plants over the growth period. T: touched, UT: untouched. *n* = 11–13 plants. H, Day of bolting of Col-0 and *mcu1 2 3* plants. T: touched, UT: untouched. Boxes extend from the 25th to 75th percentiles, the line in the box represents median, and the whiskers represent the minimum and maximum values. *n* = 11–13 plants. I, Stem height of Col-0 and *mcu1 2 3* plants 39 days after sowing. T: touched, UT: untouched. *n* = 10 plants. Error bars = SEM. J, Representative images of *mcu1 2 3* and Col-0 wild-type 27 days after sowing. T: touched, UT: untouched. K, Rosette area of *mcu1 2 3* and Col-0 wild-type plants 27 days after sowing. T: touched, UT: untouched. *n* = 11–13 plants. Error bars = SEM. Different letters indicate significant differences between all samples at *P* < 0.05 (two-way ANOVA with posthoc Tukey's test).

explore the potential importance of individual MCU isoforms in different tissues as well as potential alternative mitochondrial Ca^{2+} uptake pathways (Wagner et al., 2016; Carraretto et al., 2016a). Since the suppression of MCU was also found to impair mitochondrial Ca^{2+} transients in several animal model systems (De Stefani et al., 2011; Pan et al., 2013; Xu and Chisholm, 2014; Holmström et al., 2015; Tufi et al., 2019), the dominant role of MCU amongst the mitochondrial Ca^{2+} uptake mechanisms appears to be evolutionarily conserved among plants and metazoans.

MCUs set the baseline of plant mitochondrial free Ca^{2+} concentrations

Reduced matrix free Ca^{2+} concentrations at resting state were previously observed in *mcu* loss-of-function lines of fruit fly (*Drosophila melanogaster*) and mouse (*Mus musculus*) (Pan et al., 2013; Holmström et al., 2015; Tufi et al., 2019). An assessment of the characteristic tissue-specific pattern of resting matrix free Ca^{2+} levels in Arabidopsis root tips (Figures 1, E, 2, B, I, P, 3, B, and 4, A; Supplemental Figures S8, A and S9, A; Supplemental Movies S1–S5) (Loro et al., 2012; Wagner et al., 2015) revealed that the matrix free Ca^{2+} gradient from the division zone to the elongation zone was flattened in the absence of MCU1, MCU2, and MCU3 (Figure 3, B and C). This effect suggests that MCU-mediated Ca^{2+} uptake is a decisive factor in setting free Ca^{2+} levels even at steady-state and that this role of MCUs is evolutionary conserved between animals and plants.

Mitochondrial Ca^{2+} uptake does not shape cytosolic Ca^{2+} signatures in roots

In contrast to the mitochondrial matrix, MCU ablation had no measurable effect on cytosolic Ca^{2+} transients in Arabidopsis root tips (Figure 5; Supplemental Figure S13). Since our analysis was limited in resolution to tissue averages and due to our focus on root tips, differences in other tissues and at the cellular level or in cytosolic microdomains remain possible. In line with the observations here, the opposite situation, that is increased mitochondrial Ca^{2+} uptake capacity in Arabidopsis *micu* lines did not show any detectable impact on cytosolic Ca^{2+} dynamics either (Wagner et al., 2015). In contrast, mitochondrial Ca^{2+} uptake activity in animal systems, as mediated by the mitochondrial Ca^{2+} uniporter, was reported to act as a capacitor and to shape the cytosolic Ca^{2+} signatures, at least for specific cell types (De Stefani et al., 2011; Drago et al., 2012; Prudent et al., 2013; Rasmussen et al., 2015). Cytosolic free Ca^{2+} levels may be particularly strongly buffered to compensate for changes in Ca^{2+} sequestration activity by the mitochondria. A contribution to this buffering capacity may be made by other organelles that are known to actively participate in intracellular Ca^{2+} dynamics in plants, for example, the vacuole, the endoplasmic reticulum, and the plastids (Logan and Knight, 2003; Iwano et al., 2009; Bonza et al., 2013; Schönknecht, 2013; Loro et al., 2016; Corso et al., 2018; Sello et al., 2018; Shkolnik et al., 2018; Frank et al.,

2019; Teardo et al., 2019; Dindas et al., 2021; Resentini et al., 2021a). The impact of impaired mitochondrial Ca^{2+} transport on other organelles is beyond the scope of this study but deserves further attention, especially in the light of the observed JA-related phenotype.

Impairment of mitochondrial Ca^{2+} uniport in vivo causes a spectrum of organismal phenotypes

The biochemical properties of the mitochondrial Ca^{2+} uniporter complexes from different metazoan species have been resolved to the highest detail by X-ray and cryo-EM studies, resulting in a comprehensive understanding of the structural basis of their function and regulation (Baradaran et al., 2018; Fan et al., 2018, 2020; Nguyen et al., 2018b; Wang et al., 2019), pharmacology (Arduino et al., 2017; Paillard et al., 2018; Di Marco et al., 2020), and the functions of their components in positioning within the mitochondrial membrane (Gottschalk et al., 2019). Also, a growing number of pathologies have been linked to defects in uniporter function in mammals and other metazoans (Logan et al., 2014; Kwong et al., 2015; Mammucari et al., 2015; Antony et al., 2016; Lewis-Smith et al., 2016; Liao et al., 2017; Debattisti et al., 2019). The functional in vivo significance of the uniporter remains difficult terrain, however, and has been under debate (Murphy et al., 2014; Pendin et al., 2014). Specifically, an *mcu* knockout mouse line was viable and showed surprisingly mild phenotypes (Pan et al., 2013; Pendin et al., 2014; Holmström et al., 2015). Severe phenotypic impairment or lethality was predicted for animal models based on the function of matrix Ca^{2+} dynamics in controlling cell death pathways and respiratory activity (reviewed in [Wagner et al., 2016]). In different *mcu* mouse models, the functions of even cardiac tissues and brown fat were largely uncompromised (Luongo et al., 2015; Flicker et al., 2019). Consistently mild phenotypes were observed in response to impaired mitochondrial Ca^{2+} uptake in fruit fly (Tufi et al., 2019) and nematode (*Caenorhabditis elegans*) (Xu and Chisholm, 2014), while severe developmental defects occurred in zebrafish and *Trypanosoma brucei* lacking MCU (Huang et al., 2013; Prudent et al., 2013).

Despite the severe impairment in mitochondrial Ca^{2+} uptake and baseline maintenance in the Arabidopsis *mcu1 2 3* line, plant growth and development were not visibly compromised in the large majority of instances that we assessed (Supplemental Figures S4, B–D; S14–19; S22). The absence of an obvious organismal phenotype despite a pronounced cell physiological phenotype is reminiscent of recent observations in Arabidopsis chloroplasts lacking two POLLUX ion channel family proteins, PLASTID ENVELOPE ION CHANNEL 1 and 2 (PEC1/2) (Völkner et al., 2021). The strict retention of at least one MCU gene in genomes across the plant phylogeny indicates a selective advantage provided by MCU genes. For single loss-of-function lines of MCU1 and MCU2, impaired root growth and decreased male fertility associated with decreased in vitro pollen tube germination and growth were previously reported, respectively (Teardo

et al., 2017; Selles et al., 2018), in the absence of drastic impairment of mitochondrial Ca²⁺ uptake. We were unable to observe similar phenotypes in the *mcu1 2 3* line (Supplemental Figures S15 and S17). If the phenotypes reported for the single mutants were associated with mitochondrial Ca²⁺ uptake, the arising phenotypes may be expected to be at least the same in the *mcu1 2 3* line, where mitochondrial Ca²⁺ uptake is severely compromised. Since this was not observed, the phenotypes may be independent of Ca²⁺ transport function, and the effect may have been lost by compensation through yet unknown factors in the triple mutant. Alternatively, the reported phenotypes may arise only under specific experimental conditions, such as those in the previous studies, and those conditions may not have been replicated with the required precision here.

Although broad phenotyping efforts did not reveal major effects on growth and development of the *mcu1 2 3* line under most conditions, we observed slightly less chlorophyll degradation in response to whole plant darkening (Supplemental Figure S20). This difference is in line with the increased transcript abundance of *MCU1* and 3 that was previously observed during developmental and dark-induced senescence (Chrobok et al., 2016; Law et al., 2018). Since whole plant darkening will initially trigger a metabolic starvation response, followed by the induction of senescence (Law et al., 2018), the specific involvement of MCU in dark starvation and/or leaf senescence deserves future dissection, along with the analysis of mitochondrial Ca²⁺ dynamics in mature leaves that face this treatment. While it is not possible to comprehensively cover growth conditions, biological processes, and genotype–environment interactions, the observed phenotypes provide a handle on the physiological importance of mitochondrial Ca²⁺ transport. How exactly these phenotypes arise deserves focused analysis. Mechanistic analysis is likely to offer insight into the role of plant mitochondrial Ca²⁺ uptake in the integration of external stimuli, hormonal regulation, and growth responses.

Decreasing MCU capacity in plants selectively affects JA homeostasis

The lack of global reprogramming of the *mcu1 2 3* seedling root transcriptome (Figure 6A) is in line with the absence of obvious gross pleiotropic phenotypes under a range of conditions that we tested. Instead, the selective enrichment and concerted repression of JA-related transcripts and doubling in basal JA and JA-Ile levels hint at a link between mitochondrial Ca²⁺ dynamics and JA signaling (Figure 6, B–E; Supplemental Figure S21). It seems likely that the decreased responsiveness to touch in *mcu1 2 3* plants, as manifested by less pronounced thigmomorphogenesis responses (Figure 6, F–K), is linked to deregulated JA homeostasis. However, this hypothesis will need to be tested. The observation of increased chlorophyll content in *mcu1 2 3* rosettes after whole plant darkening (Supplemental Figure S20) might also be linked to the deregulation of JA. JA was previously found to induce leaf senescence via the repression of

Rubisco activase (Shan et al., 2011), and key photosynthetic proteins were repressed in response to wounding in a JA-dependent manner (Gfeller et al., 2011). The mechanistic nature of the unexpected link to JA, and the apparent uncoupling of the positive feedback regulation of JA, lay the groundwork for further study, especially since our understanding of the relationship between mitochondria and plant hormonal regulation is still in its infancy (Berkowitz et al., 2016). The interaction between Ca²⁺ signaling and JA-signal transduction is known to occur in the cytosol and nucleus, where JA induces Ca²⁺ mobilization to modulate the expression of JA-response genes (Sun et al., 2010; Yan et al., 2018), and CPKs as well as CBL–CIPK complexes can act as regulators of JA signaling (Munemasa et al., 2011; Förster et al., 2019). Indeed, Ca²⁺ signaling is required for the induction of JA biosynthesis (Wasternack, 2007; Toyota et al., 2018; Meena et al., 2019), and eATP signaling involving intracellular Ca²⁺ transients (as exploited in this work) was shown to affect JA signaling to optimize plant defense responses (Tripathi et al., 2018). Interestingly, basal JA pathway activity is markedly dependent on endomembrane cation flux capacities, as observed in mutants with altered activity of the Ca²⁺-regulated channel TPC1 in the tonoplast (Bonaventure et al., 2007; Lenglet et al., 2017).

Despite the lack of a similar mechanistic framework as for the relationship between Ca²⁺ and JA, mitochondria act as hubs that sense and integrate environmental and cellular signals to trigger specific responses to various stimuli to initiate signaling pathways that modulate nuclear gene expression to optimize growth and development (Ng et al., 2014). Genetic or chemical perturbations of mitochondrial functions result in transcriptional programming linked to plant hormone functions (Van Aken and Whelan, 2012; Zhang et al., 2014) and alter phytohormone levels (e.g. abscisic acid, gibberellic acid, and metabolites of the auxin indole-3-acetic acid) (Xu et al., 2019).

Conversely, several transcripts encoding mitochondrial proteins, such as OM66 and DIC2, have been found to be induced by mechanical signaling, which is largely JA-dependent, and mitochondrial metabolite levels change shortly after mechanical treatment (Aken et al., 2016). Interestingly, mechanical stimuli that trigger JA signaling were also shown to trigger characteristic mitochondrial Ca²⁺ transients in Arabidopsis seedlings (Logan and Knight, 2003; Teardo et al., 2015). Mitochondrial OM64 deficiency in rice (*Oryza sativa*) causes resistance to sucking and piercing insects by stimulating JA production and signaling (Guo et al., 2020). These findings, as well as the current findings, suggest a tight interaction between mitochondria, JA responses, and touch signaling, although the exact causality of these events remain to be determined.

The key advance of this study lies in the demonstration that a conserved mitochondrial Ca²⁺ uniporter system operates in planta and dominates matrix Ca²⁺ dynamics. Several critical questions about the role of mitochondrial

Ca²⁺ signaling in plants arise that can now be addressed due to the ability to gradually constrain mitochondrial Ca²⁺ transport capacity. Most importantly, plant Ca²⁺ signaling has been extensively studied but with a focus on transport across the plasma membrane and the tonoplast and on Ca²⁺ sensing in the cytosol and nucleus. A comprehensive understanding of cellular Ca²⁺ signaling will only be achieved, however, if we also integrate the other cell compartments into this picture (Kudla et al., 2018; Resentini et al., 2021b). Several different functions have been associated with mitochondrial Ca²⁺ transport in mammals. It will now be feasible to dissect which of those functions have been conserved and which plant-specific functions have been acquired during evolution. Already in this study we identified an unexpected connection with JA signaling and the touch response. Obvious questions to address in the future include how the MCU-JA-touch link is underpinned mechanistically and what additional downstream consequences JA deregulation may have on plant fitness.

Materials and methods

Plant lines, transformation, and culture conditions

Arabidopsis thaliana Col-0 mutant lines *mcu1* (SALK_082151 (Teardo et al., 2017)), *mcu2* (WiscDsLox393-396L9; Selles et al., 2018), and *mcu3* (SALK_019312) were obtained from the Nottingham Arabidopsis Stock Centre and validated by genotyping and sequencing. The primers used for the genotyping are listed in Supplemental Table S1. Double and triple mutants were obtained by crossing, and wild-type control lines were obtained by segregation. The generation of Col-0 lines expressing mitochondrial 4mt-YC3.6 and cytoplasmic NES-YC3.6 was described before (Krebs et al., 2012; Loro et al., 2012). The *mcu1*, *mcu1 2*, and *mcu1 2 3* lines were transformed with 4mt-YC3.6 or NES-YC3.6 using the floral dip method (Clough and Bent, 1998). For each construct, independent transgenic lines were selected based on antibiotic resistance and fluorescence. For *mcu1 2 3*, all experiments were recorded using two independent biosensor lines. To generate the 35S:MCU2 lines, Col-0 and *mcu1 2 3* plants expressing 4mt-YC3.6 were transformed by floral dip using the pB7GW2:MCU2 construct. T1 transformants of the Col-0 background were selected using BASTA resistance as a marker (5 days after germination in soil treated with BASTA 3 times every other day). Surviving individuals were assessed by genotyping for the presence of the 35S:MCU2 T-DNA. Since the *mcu1 2 3* line is already resistant to BASTA due to the presence of a BASTA resistance marker gene in the T-DNA in the endogenous MCU2 locus, BASTA application was used to enrich for individuals carrying the 35S:MCU2 insertion. Individuals that were markedly larger than the majority after BASTA application were selected and subsequently assessed by genotyping for the presence of the 35S:MCU2 T-DNA and by RT-qPCR for transgene expression.

Seeds were surface sterilized and stratified at 4°C in the dark for 2 days. Seedling culture was performed in growth

chambers set to long day conditions (16 h at 21°C and 90 μE m⁻² s⁻¹, 8 h at 17°C and darkness; Philips TL5 HO 49W/840 [MASTER] Cool White tubes). For Ca²⁺ imaging, seedlings were grown vertically for 4–5 days (Loro et al., 2012) on plates containing half-strength Murashige and Skoog medium (MS; Duchefa, Haarlem, the Netherlands [Murashige and Skoog, 1962]) supplemented with 0.1% (w/v) sucrose and 0.05% (w/v) 2-(N-morpholino)ethanesulfonic acid (MES), adjusted to pH 5.8 (KOH), and 0.8% (w/v) plant agar (Duchefa, Haarlem, the Netherlands). For RT-qPCR analysis of MCU gene expression, 14-day-old seedlings were grown vertically on half-strength MS medium supplemented with 0.1% (w/v) sucrose, 0.05% (w/v) MES and 0.8% (w/v) plant agar, pH 5.8 (KOH). For microarray experiments, RT-qPCR analyses of JA- and stress-related genes and phytohormone measurements, seedlings were cultured on a mesh in sterile hydroponics boxes (Phytatray II; Sigma-Aldrich, Darmstadt, Germany) filled with 150 mL half-strength MS medium supplemented with 0.1% (w/v) sucrose and 0.05% (w/v) MES, pH 5.8 (KOH). After 20 days, roots were separated from the shoot with a sharp blade, immediately frozen in liquid nitrogen, and stored at –80°C before RNA extraction. For subcellular localization studies of MCU3-GFP, *Agrobacterium* suspensions were infiltrated into the leaves of 4- to 5-week old *Nicotiana benthamiana* plants with a needleless syringe, and transformed areas were used for imaging after 2–4 days.

Plant phenotyping analyses

The individual culture and treatment conditions for the phenotypic analyses are described in the respective figure legends. The touch treatments to assess thigmomorphogenesis were carried out as described recently (Darwish et al., 2022).

Molecular cloning

The coding sequence of MCU3 was amplified from *Arabidopsis* Col-0 cDNA using primers from Supplemental Table S1 and inserted into the pDONR207 vector (Invitrogen, Carlsbad, CA, USA) using Gateway BP-Clonase II (Invitrogen) according to the manufacturer's instructions. Gateway LR recombination was used with destination vector pUBC-GFP-Dest (Grefen et al., 2010) to generate MCU3-GFP under the control of the UBQ10 promoter. The construct was introduced into *Agrobacterium tumefaciens* AGL1 cells by electroporation and used for transient expression in *N. benthamiana* leaves (Sparkes et al., 2006).

Analogously, to generate 35S:MCU2 lines, the MCU2 coding sequence was amplified from Col-0 cDNA using primers from Supplemental Table S1 and inserted into the pDONR207 vector (Invitrogen) using Gateway BP-Clonase II (Invitrogen) according to the manufacturer's instructions. Positive clones were confirmed by sequencing. Gateway LR recombination was used with pB7GW2 (Karimi et al., 2002) as a destination vector to place MCU2 under the control of the CaMV35S promoter. The construct was then introduced into *A. tumefaciens* C58C1 cells.

Phylogenetic analysis

The amino acid sequences of human MCU and MCUB (Uniprot ID Q8NE86 and QENWR8, respectively) were used to retrieve homologous sequences in *A. thaliana* and *M. musculus* through a BlastP search (Supplemental Data Set 1). Sequences were aligned by Muscle (Edgar, 2004) in MEGA version 6 (Tamura et al., 2013) with default parameters (Supplemental File S1) and clustered in an unrooted maximum likelihood tree using the JTT matrix-based method (Jones et al., 1992), uniform rates among sites (MEGA version 6). The tree with the highest log likelihood (−5697.26) is shown in Figure 1A. The bootstrap values indicated at the nodes were from 1,000 repetitions.

RNA extraction and RT–qPCR analysis

Total RNA was extracted from pooled shoots or roots of 20-day-old seedlings grown under hydroponic conditions or from 2-week-old seedlings vertically grown in Petri dishes using a NucleoSpin RNA Plant kit, treated with DNase I (both from Macherey-Nagel, Düren, Germany), and used for RT–qPCR analyses of JA- and stress-related genes or MCU gene expression, respectively. RNA (500 ng) was reverse transcribed using an iScript cDNA Synthesis Kit (BioRad, Hercules, CA, USA). A “no RT”-reaction, in which the RNA was subjected to the same conditions of cDNA synthesis but without reverse transcriptase, was included as a negative control in all RT–qPCR analyses. RT–qPCR was performed with SYBR Green detection (KAPA SYBR Fast qPCR Master Mix, Roche, Mannheim, Germany) in a C1000 Touch Thermal Cycler using the CFX 96 Real-Time System (Bio-Rad, Hercules, CA, USA) and specific primers (Supplemental Table S1). Data were analyzed using the DDC_T method/comparative CT method. The transcript levels were normalized to that of the SAND family protein (SAND FP, At2g28390; Czechowski et al., 2005), and the relative expression levels for each analyzed gene were determined by comparative CT methods (Schmittgen and Livak, 2008). All RT–qPCR reactions were run in triplicates using total RNA preparations from independent pools of plants that were grown side-by-side under identical experimental conditions.

Transcriptome analysis

Gene expression profiling was performed using Arabidopsis AraGene-1_0-st-type arrays from Affymetrix. RNA was extracted from the samples as described for RT–qPCR analysis from five independent replicates of pooled root tissue. Biotinylated antisense cDNA was prepared according to the Affymetrix standard labeling protocol with a GeneChip WT Plus Reagent Kit and a GeneChip Hybridization, Wash and Stain Kit (both from Affymetrix, Santa Clara, USA). Afterwards, hybridization on the chip was performed in a GeneChip Hybridization oven 640, dyed in the GeneChip Fluidics Station 450, and scanned with a GeneChip Scanner 3000. All of the equipment used was from the Affymetrix Company (Affymetrix, High Wycombe, UK).

Bioinformatic analysis of transcriptome data

A Custom CDF version 22 with TAIR based gene definitions was used to annotate the arrays (Dai et al., 2005). The raw fluorescence intensity values were normalized by applying quantile normalization and robust multichip average (RMA) background correction. An analysis of variance (ANOVA) model, using genotype and treatment as fixed effects, was performed to identify differentially expressed genes using a commercial software package (SAS JMP10 Genomics, version 6, SAS Institute, Cary, NC, USA). A false positive rate of $\alpha = 0.05$ with false discovery rate (FDR) correction was taken as the level of significance. Downregulated genes ($FC \leq -1.5$ and P -adjusted < 0.05) in *mcu1 2 3* were analyzed for gene ontology (GO) term enrichment using GOzilla (<http://cbl-gorilla.cs.technion.ac.il/>) (Eden et al., 2009).

Time lapse in vivo Ca²⁺ imaging of root tips

Four to 5-day-old seedlings were used for root imaging as optimized and described previously (Loro et al., 2012; Wagner et al., 2015; Behera et al., 2018). Briefly, seedlings were gently placed into a dedicated custom perfusion chamber and stabilized with cotton wool soaked in imaging solution (5 mM KCl, 10 mM MES, and 10 mM CaCl₂, pH 5.8 (Tris)). The root was continuously perfused with imaging solution, whereas the shoot was not submerged. The seedlings were kept under continuous perfusion for 10 min before ratiometric image acquisition as an optimization of a previous protocol (Teardo et al., 2017) in order to minimize the potential impact of specimen manipulation on the measurements. Treatments were performed by supplementing the imaging solution with 0.01 mM NAA (from a 10.74 mM stock solution) or with sodium adenosine triphosphate (Na₂ATP, working solution of 0.01, 0.1, or 2 mM from a 200 mM stock solution buffered at pH 7.4 with NaOH). The 200 mM D-sorbitol solution was prepared as described for standard imaging solution with the direct addition of the sugar powder (5 mM KCl, 10 mM MES, 10 mM CaCl₂, and 200 mM D-sorbitol, pH 5.8 (Tris)). The solutions were administered for 3 min under running perfusion and then washed out. The experiments conducted using wild-type and mutant seedlings were performed alternatingly. An inverted fluorescence microscope (Ti-E Nikon) was used for time lapse acquisition with a CFI PLAN APO 20× VC dry objective for stimulation with NAA and eATP, or a CFI Plan Fluor 4× dry objective for stimulation with D-sorbitol. Excitation light was produced by a Prior Lumen 200 PRO fluorescent lamp (Prior Scientific) at 440 nm (436/20 nm) set to 20%. Images were collected with a dual charge-coupled device camera (ORCA-D2; Hamamatsu). For Cameleon analysis, the FRET CFP/YFP optical block A11400-03 (emission 1 483/32 for CFP and emission 2 524/27 for FRET) with a dichroic 510 nm mirror (Hamamatsu) was used for the simultaneous CFP and cpVenus acquisitions. Images were acquired every 5 s. For the roots of seedlings expressing the mitochondrial Cameleon, the exposure times were 100–500 ms (depending on the magnification used) with a 4 × 4 pixel binning, while

for the cytosolic Cameleon, the exposure times were 100 ms with a 2×2 pixel binning. Filters and dichroic mirrors were from Chroma Technology. NIS-Elements (Nikon) was used as a platform to control the microscope, illuminator, and camera.

Ratiometric image data analysis

Individual ratiometric images and time-lapse imaging data were analyzed using a custom MatLab program package (Fricker, 2016). Unless otherwise indicated, the fluorescence intensity was determined over ROIs, which corresponded to the entire root tip. The cpVenus and CFP emissions of the analyzed ROIs were used for the ratio (R) calculations (cpVenus/CFP). Background subtraction was performed independently for both channels before calculating the ratio. To analyze the sorbitol treatments, we employed the Template Matching Plugin (normalized cross-correlation configuration in the Drop menu of Fiji's Matching method) for ImageJ and Fiji software. The plugin was necessary to eliminate root-tip movements due to the change in cells turgor, as determined by examining the change in the osmotic potential of the solution, hence eliminating measurement artifacts due to specimen movement.

Confocal microscopy

Confocal imaging was performed with a Leica SP5 inverted laser scanning microscope using a $25 \times$ lens (HCX IRAPO L, 0.95 numerical aperture, water immersion, zoom 1.5 was used) or a $63 \times$ lens (HCX PL APO, 1.20 numerical aperture, water immersion, zoom $10 \times$ was used). To visualize cell wall organization, roots were stained by incubating in the dark for 5 min in $1 \mu\text{g mL}^{-1}$ propidium iodide (P4864; Sigma-Aldrich, Darmstadt, Germany) solution (from a 2 mg mL^{-1} stock solution diluted in ddH₂O) and rinsed two times in water (Alassimone et al., 2010). Propidium iodide was monitored with a 514 nm excitation wavelength and a 564–660 nm bandpass emission filter. For colocalization studies with MitoTracker, plant material was submerged for 30 min with 200 nM MitoTracker Orange CMTMRos (M7510, Invitrogen). Fluorescence of cpVenus and MitoTracker was measured at 514 nm; emission was collected at 520–550 and 570–620 nm, respectively.

Confocal imaging of MCU3-GFP was performed with a Leica TCS SP8X laser scanning microscope using a $63 \times$ lens (HC PL APO CS2, 1.20 numerical aperture, water immersion). GFP and chlorophyll were excited at 488 nm using a flexible pulsed white-light laser, and emission was collected using hybrid detectors at 505–530 and 650–700 nm, respectively. Minor chloroplastic signal in the GFP channel was observed when using standard confocal microscopy settings as described in a previous report (Carraretto et al., 2016b) but was entirely removed by the time gating function of the microscope, which allows fluorophores to be separated out based on their fluorescence lifetimes. For the data shown in Supplemental Figure S5, GFP detection was time-gated at 0.3–12.0 ns (Kodama, 2016).

Photosynthetic efficiency

Measurements of efficiency of photosystem II (F_v/F_m) were performed on true leaves of 32-day-old plants as described previously (Teardo et al., 2017).

Phytohormone measurements

Measurements of OPDA, dnOPDA, JA, and JA-Ile were performed on roots of 20-day-old seedlings grown on mesh in sterile hydroponics boxes. Phytohormones were quantified simultaneously using a standardized Ultra-performance liquid chromatography–tandem Mass Spectrometry (UPLC–MS/MS)-based method according to Balcke et al. (2012). In brief, 50 mg of frozen samples were extracted with 500 μL methanol supplied with [²H₅]OPDA, [²H₆]JA, and [²H₂]JA-Ile (50 ng each) as internal standards. After centrifugation, the supernatant was diluted with nine volumes of water and subjected to solid phase extraction on HR-XC (Chromabond, Macherey-Nagel, Düren, Germany). Elution was done with 900 μL acetonitrile, and 10 μL of the eluate were subjected to UPLC–MS/MS. The phytohormone contents were calculated using the ratio of analyte and internal standard peak heights, thereby calculating the content of dnOPDA using [²H₅]OPDA as an internal standard.

Immunoblotting

Proteins were extracted from frozen seedling tissue (50 mg) by adding 200 μL of extraction buffer (25 mM Tris–Cl pH 6.8, 1% SDS, 1% (v/v) β -mercaptoethanol, 1% (v/v) Halt protease inhibitor cocktail [Sigma-Aldrich, #78442]) and heating at 95°C for 5 min. After centrifugation for 10 min, the supernatant was collected and proteins quantified using Coomassie Plus Reagent (Sigma-Aldrich, #23236). Ten microgram total protein was mixed with $2 \times$ Laemmli Buffer (1:1) and heated at 96°C for 10 min to dissolve AOC trimers. Proteins were separated by SDS–PAGE (12% acrylamide) and transferred to a PVDF membrane. Detection of protein bands was done by staining with Ponceau S. The membrane was blocked with 5% (w/v) BSA in TBST (20 mM Tris–Cl pH 7.8, 150 mM NaCl, 0.05% [v/v] Tween) and immunostained using anti-AtAOC antibody (1:5,000, Stenzel et al., 2003) and a goat anti-rabbit IgG antibody conjugated with alkaline phosphatase (1:5,000, Sigma-Aldrich). Chemiluminescence detection was performed with ImmunoStar AP Substrate (ThermoFisher Scientific, Waltham, MA, USA, #1705018) for 5 min and visualized using a Fusion FX Imaging system (Vilber, www.vilber.com).

Statistical analysis

The statistical analyses applied to the individual datasets are detailed in the respective figure legends, and a summary is provided in Supplemental Data Set 5. All statistical tests were conducted using Microsoft Excel and GraphPad Prism.

Accession numbers

Sequence data from this article can be found in the GenBank/EMBL libraries under the following accession numbers: AGC2-1, At3g25250; AOS, At5g42650; CPK28,

At5g66210; GRX480, At1g28480; LOX3, At1g17420; JAZ1, At1g19180; JAZ2, At1g74950; JAZ3, At3g17860; JAZ5, At1g17380; JAZ6, At1g72450; JAZ8, At1g30135; JAZ9, AT5G20900; JAZ10, At5g13220; JAZ12, At1g70700; MCU1, At1g09575; MCU2, At1g57610; MCU3, At2g23790; MCU4, At4g36820; MCU5, At5g42610; MCU6, At5g66650; MYC2, At1Gg32640; NPR3, At5g45110; OPR3, At2g06050; SAND family protein, At2g28390; WRKY40, At1g80840; WRKY53, At4g23810; UBC21, At5g25760; UBQ10, and At4g05320.

The raw and normalized transcriptome data shown in Figure 6 and Supplemental Figure S21 were deposited into the Gene Expression Omnibus database (<http://www.ncbi.nlm.nih.gov/geo/>; accession no. GSE152581).

Supplemental data

The following materials are available in the online version of this article.

Supplemental Figure S1. Protein alignment and predicted topology of MCUs in *A. thaliana*.

Supplemental Figure S2. Generation and validation of the *mcu1 2 3* line.

Supplemental Figure S3. Subcellular localization of 4mt-YC3.6 in Col-0 and *mcu1 2 3*.

Supplemental Figure S4. Primary root tip architecture is unchanged in *mcu1 2 3* seedlings.

Supplemental Figure S5. MCU3-GFP localizes to mitochondria in *N. benthamiana* epidermal cells.

Supplemental Figure S6. Generation and validation of the *mcu1 2 3* line.

Supplemental Figure S7. Subcellular localization of 4mt-YC3.6 in *mcu1 2 3*.

Supplemental Figure S8. The mitochondrial matrix Ca²⁺ transient triggered by 0.1 mM eATP shows progressive impairment with progressive ablation of MCUs.

Supplemental Figure S9. The mitochondrial matrix Ca²⁺ transient triggered by 0.01 mM eATP shows progressive impairment with progressive ablation of MCUs.

Supplemental Figure S10. The mitochondrial matrix Ca²⁺ transients induced by 0.01 mM NAA or 200 mM D-sorbitol show consistent impairment in *mcu1 2 3* compared to Col-0 as for other stimuli.

Supplemental Figure S11. Generation and validation of 35S:MCU2 lines.

Supplemental Figure S12. The mitochondrial matrix Ca²⁺ transient triggered by 2.0 mM eATP in root tips of *mcu3* and 35S:MCU2 lines.

Supplemental Figure S13. Cytosolic Ca²⁺ transients in root tips induced by treatment with 2.0 mM eATP are unchanged for all ROIs in *mcu1 2 3*.

Supplemental Figure S14. Gross plant development is unchanged in *mcu1 2 3*.

Supplemental Figure S15. Seedling development shows no obvious changes in *mcu1 2 3*.

Supplemental Figure S16. Primary root growth shows no obvious changes in *mcu1 2 3* under different external treatments.

Supplemental Figure S17. Pollen tube germination and growth, and root hair development are unchanged in *mcu1 2 3*.

Supplemental Figure S18. *mcu1 2 3* and Col-0 seedling growth in the presence of antimycin A (AA).

Supplemental Figure S19. Submergence and low oxygen responses in Col-0 and *mcu1 2 3* plants.

Supplemental Figure S20. Whole plant darkening to induce starvation and senescence in Col-0 and *mcu1 2 3* plants.

Supplemental Figure S21. Repression of JA homeostasis in *mcu1 2 3* seedlings.

Supplemental Figure S22. Root penetration growth of Col-0 and *mcu1 2 3* in media with different agar concentrations.

Supplemental Table S1. List of primers.

Supplemental Data Set 1. Sequence information used for phylogenetic analysis.

Supplemental Data Set 2. List of 159 downregulated genes in *mcu1 2 3* compared to Col-0.

Supplemental Data Set 3. List of 13 upregulated genes in *mcu1 2 3* compared to Col-0.

Supplemental Data Set 4. List of 14 genes repressed in *mcu1 2 3* and present in the MYC2 regulon dataset.

Supplemental Data Set 5. Summary of statistical analyses.

Supplemental File S1. Sequence alignments for phylogenetic analysis.

Supplemental File S2. MCU transcript abundance in different Arabidopsis organs and during development as observed in publicly available transcriptome analyses and curated by the Genevestigator platform.

Supplemental Movie S1. Mitochondrial Ca²⁺ transients in response to stimulation for 3 min with 0.01 mM NAA in living Arabidopsis root tips of Col-0, *mcu1*, and *mcu1 2*.

Supplemental Movie S2. Mitochondrial Ca²⁺ transients in response to stimulation for 3 min with 0.01 mM eATP in living Arabidopsis root tips of Col-0, *mcu1*, and *mcu1 2*.

Supplemental Movie S3. Mitochondrial Ca²⁺ transients in response to stimulation for 3 min with 0.10 mM eATP in living Arabidopsis root tips of Col-0, *mcu1*, and *mcu1 2*.

Supplemental Movie S4. Mitochondrial Ca²⁺ transients in response to stimulation for 3 min with 2.0 mM eATP in living Arabidopsis root tips of Col-0, *mcu1*, and *mcu1 2*.

Supplemental Movie S5. Mitochondrial Ca²⁺ transients in response to stimulation for 3 min with 2.0 mM eATP in living Arabidopsis root tips of Col-0 and *mcu1 2 3*.

Supplemental Movie S6. Cytosolic Ca²⁺ transients in response to stimulation for 3 min with 2.0 mM eATP in living Arabidopsis root tips of Col-0 and *mcu1 2 3*.

Acknowledgments

We are grateful for the access to the Leica SP5 and SP8 confocal microscope systems as maintained by Jörg Kudla (Münster) and the Imaging Network of the University of Münster (RI_00497). We thank Olivier Keech (Umea), Andreas Meyer (Bonn), Ildikó Szabó (Padova), Michela

Zottini (Padova), Anna Fedyeva (Irkutsk), Alina Griese (Münster), Felix Nowack (Ghent), Christopher Grefen (Bochum), Ute Vothknecht (Bonn), Hassan Ghareeb (Göttingen), Andrea Magni (Milan) and Volker Lipka (Göttingen) for fruitful discussions and/or preliminary experimental explorations. We further thank Hagen Stellmach (IPB Halle) for technical support with the phytohormone measurements.

Funding

M.S. thanks the Deutsche Forschungsgemeinschaft for funding through the Emmy-Noether programme (SCHW1719/1-1), the Research Training Group 2064 “Water use efficiency and drought stress responses: From Arabidopsis to Barley”, the infrastructure grants INST211/903-1 FUGG and INST 211/853-1 FUGG, and a project grant (SCHW1719/5-1) as part of the package PAK918. This work was supported by PIANO DI SVILUPPO DI ATENEO 2019 (Università degli Studi di Milano) to A.C., a fellowship by the National Natural Science Foundation of China to Z.X. (31701454; project number 31800312), a PhD fellowship from the University of Milan to M.G., a fellowship of the University of Antwerp to S.S. (DOCPRO4), of the Research Foundation Flanders (FWO-Vlaanderen) to K.V. O.V.A. was supported by the Swedish Research Council (Vetenskapsrådet 2017-03854) and Carl Trygger Foundation (CTS 17: 487). B.H. and K.M. were supported by a grant from the Deutsche Forschungsgemeinschaft (GRK2498-400681449).

Conflict of interest statement. None declared.

References

- Aken OV, Clercq ID, Ivanova A, Law SR, Breusegem FV, Millar AH, Whelan J (2016) Mitochondrial and chloroplast stress responses are modulated in distinct touch and chemical inhibition phases. *Plant Physiol* **171**: 2150–2165
- Alassimone J, Naseer S, Geldner N (2010) A developmental framework for endodermal differentiation and polarity. *Proc Natl Acad Sci USA* **107**: 5214–5219
- Antony AN, Paillard M, Moffat C, Juskeviciute E, Correnti J, Bolon B, Rubin E, Csordás G, Seifert EL, Hoek JB, et al. (2016) MICU1 regulation of mitochondrial Ca^{2+} uptake dictates survival and tissue regeneration. *Nat Commun* **7**: 10955
- Arduino DM, Wettmarshausen J, Vais H, Navas-Navarro P, Cheng Y, Leimpek A, Ma Z, Delrio-Lorenzo A, Giordano A, Garcia-Perez C, et al. (2017) Systematic identification of MCU modulators by orthogonal interspecies chemical screening. *Mol Cell* **67**: 711–723.e7
- Balcke GU, Handrick V, Bergau N, Fichtner M, Henning A, Stellmach H, Tissier A, Hause B, Frolov A (2012) An UPLC-MS/MS method for highly sensitive high-throughput analysis of phytohormones in plant tissues. *Plant Methods* **8**: 47
- Baradaran R, Wang C, Siliciano AF, Long SB (2018) Cryo-EM structures of fungal and metazoan mitochondrial calcium uniporters. *Nature* **559**: 580–584
- Baughman JM, Perocchi F, Girgis HS, Plovanich M, Belcher-Timme CA, Sancak Y, Bao XR, Strittmatter L, Goldberger O, Bogorad RL, et al. (2011) Integrative genomics identifies MCU as an essential component of the mitochondrial calcium uniporter. *Nature* **476**: 341–345
- Beaugelin I, Chevalier A, D’Alessandro S, Ksas B, Novák O, Strnad M, Forzani C, Hirt H, Havaux M, Monnet F (2019) OX11 and DAD regulate light-induced cell death through jasmonate and salicylate levels. *Plant Physiol* **180**: 1691–1708
- Behera S, Xu Z, Luoni L, Bonza MC, Doccula FG, De Michelis MI, Morris RJ, Schwarzländer M, Costa A (2018) Cellular Ca^{2+} signals generate defined pH signatures in plants. *Plant Cell* **30**: 2704–2719
- Berkowitz O, De Clercq I, Van Breusegem F, Whelan J (2016) Interaction between hormonal and mitochondrial signalling during growth, development and in plant defence responses. *Plant Cell Environ* **39**: 1127–1139
- Bick AG, Calvo SE, Mootha VK (2012) Evolutionary diversity of the mitochondrial calcium uniporter. *Science* **336**: 886
- Bonaventure G, Gfeller A, Proebsting WM, Hörtensteiner S, Chételat A, Martinoia E, Farmer EE (2007) A gain-of-function allele of TPC1 activates oxylipin biogenesis after leaf wounding in Arabidopsis. *Plant J* **49**: 889–898
- Bondarenko AI, Jean-Quartier C, Malli R, Graier WF (2013) Characterization of distinct single-channel properties of Ca^{2+} inward currents in mitochondria. *Pflügers Arch* **465**: 997–1010
- Bonza MC, Loro G, Behera S, Wong A, Kudla J, Costa A (2013) Analyses of Ca^{2+} accumulation and dynamics in the endoplasmic reticulum of Arabidopsis root cells using a genetically encodedameleon sensor. *Plant Physiol* **163**: 1230–1241
- Buntinas L, Gunter KK, Sparagna GC, Gunter TE (2001) The rapid mode of calcium uptake into heart mitochondria (RaM): comparison to RaM in liver mitochondria. *Biochim Biophys Acta (BBA) - Bioenerget* **1504**: 248–261
- Caarls L, Elberse J, Awwanah M, Ludwig NR, de Vries M, Zeilmaker T, Van Wees SCM, Schuurink RC, Van den Ackerveken G (2017) Arabidopsis JASMONATE-INDUCED OXYGENASES down-regulate plant immunity by hydroxylation and inactivation of the hormone jasmonic acid. *Proc Natl Acad Sci USA* **114**: 6388–6393
- Carafoli E, Krebs J (2016) Why calcium? How calcium became the best communicator. *J Biol Chem* **291**: 20849–20857
- Carraretto L, Checchetto V, De Bortoli S, Formentin E, Costa A, Szabó I, Teardo E (2016a) Calcium flux across plant mitochondrial membranes: possible molecular players. *Front Plant Sci* **7**: 354
- Carraretto L, Teardo E, Checchetto V, Finazzi G, Uozumi N, Szabo I (2016b) Ion channels in plant bioenergetic organelles, chloroplasts and mitochondria: from molecular identification to function. *Mol Plant* **9**: 371–395
- Charpentier M, Sun J, Vaz Martins T, Radhakrishnan GV, Findlay K, Soumpourou E, Thouin J, Véry A-A, Sanders D, Morris RJ, et al. (2016) Nuclear-localized cyclic nucleotide-gated channels mediate symbiotic calcium oscillations. *Science* **352**: 1102–1105
- Chiarillo MA, Lander N, Bertolini MS, Storey M, Vercesi AE, Docampo R (2017) Different roles of mitochondrial calcium uniporter complex subunits in growth and infectivity of *Trypanosoma cruzi*. *mBio* **8**: e00574-17
- Chrobok D, Law SR, Brouwer B, Linden P, Ziolkowska A, Liebsch D, Narsai R, Szal B, Moritz T, Rouhier N, et al. (2016) Dissecting the metabolic role of mitochondria during developmental leaf senescence. *Plant Physiol* **172**: 2132–2153
- Clough SJ, Bent AF (1998) Floral dip: a simplified method for *Agrobacterium*-mediated transformation of *Arabidopsis thaliana*. *Plant J* **16**: 735–743
- Corso M, Doccula FG, de Melo JRF, Costa A, Verbruggen N (2018) Endoplasmic reticulum-localized CCX2 is required for osmotolerance by regulating ER and cytosolic Ca^{2+} dynamics in Arabidopsis. *Proc Natl Acad Sci USA* **115**: 3966–3971
- Czechowski T, Stitt M, Altmann T, Udvardi MK, Scheible WR (2005) Genome-wide identification and testing of superior reference genes for transcript normalization in Arabidopsis. *Plant Physiol* **139**: 5–17
- Dai M, Wang P, Boyd AD, Kostov G, Athey B, Jones EG, Bunney WE, Myers RM, Speed TP, Akil H, et al. (2005) Evolving gene/

- transcript definitions significantly alter the interpretation of GeneChip data. *Nucleic Acids Res* **33**: e175
- Darwish E, Ghosh R, Ontiveros-Cisneros A, Tran HC, Petersson M, De Milde L, Broda M, Goossens A, Van Moerkercke A, Khan K, et al.** (2022). Touch signaling and thigmomorphogenesis are regulated by complementary CAMTA3- and JA-dependent pathways. *Sci Adv* **8**: eabm2091
- De Clercq I, Vermeirssen V, Van Aken O, Vandepoele K, Murcha MW, Law SR, Inze A, Ng S, Ivanova A, Rombaut D, et al.** (2013). The membrane-bound NAC transcription factor ANAC013 functions in mitochondrial retrograde regulation of the oxidative stress response in *Arabidopsis*. *Plant Cell* **25**: 3472–3490
- De Stefani D, Raffaello A, Teardo E, Szabò I, Rizzuto R** (2011) A forty-kilodalton protein of the inner membrane is the mitochondrial calcium uniporter. *Nature* **476**: 336–340
- Debattisti V, Horn A, Singh R, Seifert EL, Hogarth MW, Mazala DA, Huang KT, Horvath R, Jaiswal JK, Hajnóczky G** (2019) Dysregulation of mitochondrial Ca²⁺ uptake and sarcolemma repair underlie muscle weakness and wasting in patients and mice lacking MICU1. *Cell Rep* **29**: 1274–1286.e6
- DeLuca HF, Engstrom GW** (1961) Calcium uptake by rat kidney mitochondria. *Proc Natl Acad Sci USA* **47**: 1744–1750
- Deng Y, Srivastava R, Quilichini TD, Dong H, Bao Y, Horner HT, Howell SH** (2016) IRE1, a component of the unfolded protein response signaling pathway, protects pollen development in *Arabidopsis* from heat stress. *Plant J* **88**: 193–204
- Di Marco G, Vallese F, Jourde B, Bergsdorf C, Sturlese M, De Mario A, Techer-Etienne V, Haasen D, Oberhauser B, Schleeper S, et al.** (2020) A high-throughput screening identifies MICU1 targeting compounds. *Cell Rep* **30**: 2321–2331.e6
- Dieter P, Marmé D** (1980) Ca²⁺ transport in mitochondrial and microsomal fractions from higher plants. *Planta* **150**: 1–8
- Dindas J, Dreyer I, Huang S, Hedrich R, Roelfsema MRG** (2021) A voltage-dependent Ca²⁺ homeostat operates in the plant vacuolar membrane. *New Phytol* **230**: 1449–1460
- Drago I, De Stefani D, Rizzuto R, Pozzan T** (2012) Mitochondrial Ca²⁺ uptake contributes to buffering cytoplasmic Ca²⁺ peaks in cardiomyocytes. *Proc Natl Acad Sci USA* **109**: 12986–12991
- Edel KH, Marchadier E, Brownlee C, Kudla J, Hetherington AM** (2017) The evolution of calcium-based signalling in plants. *Curr Biol* **27**: R667–R679
- Eden E, Navon R, Steinfeld I, Lipson D, Yakhini Z** (2009) GOrilla: a tool for discovery and visualization of enriched GO terms in ranked gene lists. *BMC Bioinformatics* **10**: 48
- Edgar RC** (2004) MUSCLE: multiple sequence alignment with high accuracy and high throughput. *Nucleic Acids Res* **32**: 1792–1797
- Elías J, Yáñez M, Pereira TMC, Gil-Longo J, MacDougall DA, Campos-Toimil M** (2020) An update to calcium binding proteins. *Adv Exp Med Biol* **1131**: 183–213
- Fan C, Fan M, Orlando BJ, Fastman NM, Zhang J, Xu Y, Chambers MG, Xu X, Perry K, Liao M, et al.** (2018) X-ray and cryo-EM structures of the mitochondrial calcium uniporter. *Nature* **559**: 575–579
- Fan M, Zhang J, Tsai CW, Orlando BJ, Rodriguez M, Xu Y, Liao M, Tsai MF, Feng L** (2020) Structure and mechanism of the mitochondrial Ca²⁺ uniporter holocomplex. *Nature* **582**: 129–133
- Flicker D, Sancak Y, Mick E, Goldberger O, Mootha VK** (2019) Exploring the *in vivo* role of the mitochondrial calcium uniporter in brown fat bioenergetics. *Cell Rep* **27**: 1364–1375.e5
- Förster S, Schmidt LK, Kopic E, Anschütz U, Huang S, Schlücking K, Köster P, Waadt R, Larrieu A, Batistić O, et al.** (2019) Wounding-induced stomatal closure requires jasmonate-mediated activation of GORK K⁺ channels by a Ca²⁺ sensor-kinase CBL1-CIPK5 complex. *Dev Cell* **48**: 87–99.e6
- Frank J, Happeck R, Meier B, Hoang MTT, Stribny J, Hause G, Ding H, Morsomme P, Baginsky S, Peiter E** (2019) Chloroplast-localized BICAT proteins shape stromal calcium signals and are required for efficient photosynthesis. *New Phytol* **221**: 866–880
- Fricker MD** (2016) Quantitative redox imaging software. *Antioxid Redox Signal* **24**: 752–762
- Fuchs P, Bohle F, Lichtenauer S, Ugalde JM, Feitosa Araujo E, Mansuroglu B, Ruberti C, Wagner S, Muller-Schussele SJ, Meyer AJ, et al.** (2022). Reductive stress triggers ANAC017-mediated retrograde signaling to safeguard the endoplasmic reticulum by boosting mitochondrial respiratory capacity. *Plant Cell* **34**: 1375–1395
- Fuchs P, Rugen N, Carrie C, Elsässer M, Finkemeier I, Giese J, Hildebrandt TM, Kühn K, Maurino VG, Ruberti C, et al.** (2020) Single organelle function and organization as estimated from *Arabidopsis* mitochondrial proteomics. *Plant J* **101**: 420–441
- Gfeller A, Baerenfaller K, Loscos J, Chetelat A, Baginsky S, Farmer EE** (2011) Jasmonate controls polypeptide patterning in undamaged tissue in wounded *Arabidopsis* leaves. *Plant Physiol* **156**: 1797–1807
- Gottschalk B, Klec C, Leitinger G, Bernhart E, Rost R, Bischof H, Madreiter-Sokolowski CT, Radulović S, Eroglu E, Sattler W, et al** (2019) MICU1 controls cristae junction and spatially anchors mitochondrial Ca²⁺ uniporter complex. *Nat Commun* **10**: 3732
- Grefen C, Donald N, Hashimoto K, Kudla J, Schumacher K, Blatt MR** (2010) A ubiquitin-10 promoter-based vector set for fluorescent protein tagging facilitates temporal stability and native protein distribution in transient and stable expression studies. *Plant J* **64**: 355–365
- Greenzi M, Resentini F, Vanneste S, Zottini M, Bassi A, Costa A** (2021) Illuminating the hidden world of calcium ions in plants with a universe of indicators. *Plant Physiol* **187**: 550–571
- Guo HM, Li HC, Zhou SR, Xue HW, Miao XX** (2020) Deficiency of mitochondrial outer membrane protein 64 confers rice resistance to both piercing-sucking and chewing insects in rice. *J Integr Biol* **62**: 1967–1982
- Hajnóczky G, Csordás G** (2010) Calcium signalling: fishing out molecules of mitochondrial calcium transport. *Curr Biol* **20**: R888–R891
- Hedrich R** (2012) Ion channels in plants. *Physiol Rev* **92**: 1777–1811
- Hodges TK, Hanson JB** (1965) Calcium accumulation by maize mitochondria. *Plant Physiol* **40**: 101–109
- Holmström KM, Pan X, Liu JC, Menazza S, Liu J, Nguyen TT, Pan H, Parks RJ, Anderson S, Noguchi A, et al.** (2015) Assessment of cardiac function in mice lacking the mitochondrial calcium uniporter. *J Mol Cell Cardiol* **85**: 178–182
- Hou C, Tian W, Kleist T, He K, Garcia V, Bai F, Hao Y, Luan S, Li L** (2014) DUF221 proteins are a family of osmosensitive calcium-permeable cation channels conserved across eukaryotes. *Cell Res* **24**: 632–635
- Hruz T, Laule O, Szabo G, Wessendorp F, Bleuler S, Oertle L, Widmayer P, Gruissem W, Zimmermann P** (2008) Genevestigator v3: a reference expression database for the meta-analysis of transcriptomes. *Adv Bioinformatics* **2008**: 420747
- Huang G, Vercesi AE, Docampo R** (2013) Essential regulation of cell bioenergetics in *Trypanosoma brucei* by the mitochondrial calcium uniporter. *Nat Commun* **4**: 2865
- Huang H, Liu B, Liu L, Song S** (2017) Jasmonate action in plant growth and development. *J Exp Bot* **68**: 1349–1359
- Igamberdiev AU, Hill RD** (2018) Elevation of cytosolic Ca²⁺ in response to energy deficiency in plants: the general mechanism of adaptation to low oxygen stress. *Biochem J* **475**: 1411–1425
- Iwano M, Entani T, Shiba H, Kakita M, Nagai T, Mizuno H, Miyawaki A, Shoji T, Kubo K, Isogai A, et al.** (2009) Fine-tuning of the cytoplasmic Ca²⁺ concentration is essential for pollen tube growth. *Plant Physiol* **150**: 1322–1334
- Jin H, Hong Z, Su W, Li J** (2009) A plant-specific calreticulin is a key retention factor for a defective brassinosteroid receptor in the endoplasmic reticulum. *Proc Natl Acad Sci USA* **106**: 13612–13617
- Jones DT, Taylor WR, Thornton JM** (1992) The rapid generation of mutation data matrices from protein sequences. *Comput Appl Biosci* **8**: 275–282

- Karimi M, Inze D, Depicker A (2002). GATEWAY vectors for Agrobacterium-mediated plant transformation. *Trends Plant Sci* 7: 193–195
- Kirichok Y, Krapivinsky G, Clapham DE (2004) The mitochondrial calcium uniporter is a highly selective ion channel. *Nature* 427: 360–364
- Klepikova AV, Kasianov AS, Gerasimov ES, Logacheva MD, Penin AA (2016) A high resolution map of the *Arabidopsis thaliana* developmental transcriptome based on RNA-seq profiling. *Plant J* 88: 1058–1070
- Kodama Y (2016) Time gating of chloroplast autofluorescence allows clearer fluorescence imaging in planta. *PLoS One* 11: e0152484
- Kong X, Xu L, Jamieson P (2020) Plant sense: the rise of calcium channels. *Trends Plant Sci* 25: 838–841
- Kovács-Bogdán E, Sancak Y, Kamer KJ, Plovanich M, Jambhekar A, Huber RJ, Myre MA, Blower MD, Mootha VK (2014) Reconstitution of the mitochondrial calcium uniporter in yeast. *Proc Natl Acad Sci USA* 111: 8985–8990
- Krebs M, Held K, Binder A, Hashimoto K, Den Herder G, Parniske M, Kudla J, Schumacher K (2012) FRET-based genetically encoded sensors allow high-resolution live cell imaging of Ca^{2+} dynamics. *Plant J* 69: 181–192
- Kudla J, Becker D, Grill E, Hedrich R, Hippler M, Kummer U, Parniske M, Romeis T, Schumacher K (2018) Advances and current challenges in calcium signaling. *New Phytol* 218: 414–431
- Kwong JQ, Lu X, Correll RN, Schwanekamp JA, Vagnozzi RJ, Sargent MA, York AJ, Zhang J, Bers DM, Molkentin JD (2015) The mitochondrial calcium uniporter selectively matches metabolic output to acute contractile stress in the heart. *Cell Rep* 12: 15–22
- Law SR, Chrobok D, Juvany M, Delhomme N, Linden P, Brouwer B, Ahad A, Moritz T, Jansson S, Gardstrom P, et al. (2018). Darkened leaves use different metabolic strategies for senescence and survival. *Plant Physiol* 177: 132–150
- Lee Y, Min CK, Kim TG, Song HK, Lim Y, Kim D, Shin K, Kang M, Kang JY, Youn HS, et al. (2015) Structure and function of the N-terminal domain of the human mitochondrial calcium uniporter. *EMBO Rep* 16: 1318–1333
- Leitão N, Dangeville P, Carter R, Charpentier M (2019) Nuclear calcium signatures are associated with root development. *Nat Commun* 10: 4865
- Lenglet A, Jaślan D, Toyota M, Mueller M, Müller T, Schönknecht G, Marten I, Gilroy S, Hedrich R, Farmer EE (2017) Control of basal jasmonate signalling and defence through modulation of intracellular cation flux capacity. *New Phytol* 216: 1161–1169
- Lewis-Smith D, Kamer KJ, Griffin H, Childs A-M, Pysden K, Titov D, Duff J, Pyle A, Taylor RW, Yu-Wai-Man P, et al. (2016) Homozygous deletion in MICU1 presenting with fatigue and lethargy in childhood. *Neurol Genet* 2: e59
- Liao Y, Dong Y, Cheng J (2017) The function of the mitochondrial calcium uniporter in neurodegenerative disorders. *Int J Mol Sci* 18: 248
- Logan CV, Szabadkai G, Sharpe JA, Parry DA, Torelli S, Childs A-M, Kriek M, Phadke R, Johnson CA, Roberts NY, et al. (2014) Loss-of-function mutations in MICU1 cause a brain and muscle disorder linked to primary alterations in mitochondrial calcium signaling. *Nat Genet* 46: 188–193
- Logan DC, Knight MR (2003) Mitochondrial and cytosolic calcium dynamics are differentially regulated in plants. *Plant Physiol* 133: 21–24
- Loro G, Drago I, Pozzan T, Schiavo FL, Zottini M, Costa A (2012) Targeting of Cameleons to various subcellular compartments reveals a strict cytoplasmic/mitochondrial Ca^{2+} handling relationship in plant cells. *Plant J* 71: 1–13
- Loro G, Wagner S, Doccula FG, Behera S, Weinl S, Kudla J, Schwarzländer M, Costa A, Zottini M (2016) Chloroplast-specific in vivo Ca^{2+} imaging using yellowameleon fluorescent protein sensors reveals organelle-autonomous Ca^{2+} signatures in the stroma. *Plant Physiol* 171: 2317–2330
- Luongo TS, Lambert JP, Yuan A, Zhang X, Gross P, Song J, Shanmughapriya S, Gao E, Jain M, Houser SR, et al. (2015) The mitochondrial calcium uniporter matches energetic supply with cardiac workload during stress and modulates permeability transition. *Cell Rep* 12: 23–34
- Mammucari C, Gherardi G, Zamparo I, Raffaello A, Boncompagni S, Chemello F, Cagnin S, Braga A, Zanin S, Pallafacchina G, et al. (2015) The mitochondrial calcium uniporter controls skeletal muscle trophism *in vivo*. *Cell Rep* 10: 1269–1279
- Matthus E, Sun J, Wang L, Bhat MG, Mohammad-Sidik AB, Wilkins KA, Leblanc-Fournier N, Legué V, Moulia B, Stacey G, et al. (2019) DORN1/P2K1 and purino-calcium signalling in plants: making waves with extracellular ATP. *Ann Bot* 124: 1227–1242
- McAinsh MR, Pittman JK (2009) Shaping the calcium signature. *New Phytol* 181: 275–294
- Meena MK, Prajapati R, Krishna D, Divakaran K, Pandey Y, Reichelt M, Mathew MK, Boland W, Mithöfer A, Vadassery J (2019) The Ca^{2+} channel CNGC19 regulates *Arabidopsis* defense against *Spodoptera* herbivory. *Plant Cell* 31: 1539–1562
- Mergner J, Frejno M, List M, Papacek M, Chen X, Chaudhary A, Samaras P, Richter S, Shikata H, Messerer M, et al. (2020) Mass-spectrometry-based draft of the *Arabidopsis* proteome. *Nature* 579: 409–414
- Monshausen GB, Messerli MA, Gilroy S (2008) Imaging of the yellowameleon 3.6 indicator reveals that elevations in cytosolic Ca^{2+} follow oscillating increases in growth in root hairs of *Arabidopsis*. *Plant Physiol* 147: 1690–1698
- Mousavi SAR, Dubin AE, Zeng WZ, Coombs AM, Do K, Ghadiri DA, Keenan WT, Ge C, Zhao Y, Patapoutian A (2021) PIEZO ion channel is required for root mechanotransduction in *Arabidopsis thaliana*. *Proc Natl Acad Sci USA* 118: e2102188118
- Mueller MJ (1997) Enzymes involved in jasmonic acid biosynthesis. *Physiol Plant* 100: 653–663
- Munemasa S, Hossain MA, Nakamura Y, Mori IC, Murata Y (2011) The *Arabidopsis* calcium-dependent protein kinase, CPK6, functions as a positive regulator of methyl jasmonate signaling in guard cells. *Plant Physiol* 155: 553–561
- Murashige T, Skoog F (1962) A revised medium for rapid growth and bio assays with tobacco tissue cultures. *Physiol Plant* 15: 473–497
- Murphy E, Pan X, Nguyen T, Liu J, Holmström KM, Finkel T (2014) Unresolved questions from the analysis of mice lacking MCU expression. *Biochem Biophys Res Commun* 449: 384–385
- Murthy SE, Dubin AE, Whitwam T, Jojoa-Cruz S, Cahalan SM, Mousavi SAR, Ward AB, Patapoutian A (2018) OSCA/TMEM63 are an evolutionarily conserved family of mechanically activated ion channels. *eLife* 7: e41844
- Nakagawa Y, Katagiri T, Shinozaki K, Qi Z, Tatsumi H, Furuichi T, Kishigami A, Sokabe M, Kojima I, Sato S, et al. (2007) *Arabidopsis* plasma membrane protein crucial for Ca^{2+} influx and touch sensing in roots. *Proc Natl Acad Sci USA* 104: 3639–3644
- Ng S, De Clercq I, Van Aken O, Law SR, Ivanova A, Willems P, Giraud E, Van Breusegem F, Whelan J (2014) Anterograde and retrograde regulation of nuclear genes encoding mitochondrial proteins during growth, development, and stress. *Mol Plant* 7: 1075–1093
- Nguyen CT, Kurenda A, Stolz S, Chételat A, Farmer EE (2018a) Identification of cell populations necessary for leaf-to-leaf electrical signaling in a wounded plant. *Proc Natl Acad Sci USA* 115: 10178–10183
- Nguyen NX, Armache JP, Lee C, Yang Y, Zeng W, Mootha VK, Cheng Y, Bai XC, Jiang Y (2018b) Cryo-EM structure of a fungal mitochondrial calcium uniporter. *Nature* 559: 570–574
- Paillard M, Csordás G, Huang K-T, Várnai P, Joseph SK, Hajnóczky G (2018) MICU1 interacts with the D-ring of the MCU pore to control its Ca^{2+} flux and sensitivity to Ru360. *Mol Cell* 72: 778–785.e3

- Pan X, Liu J, Nguyen T, Liu C, Sun J, Teng Y, Fergusson MM, Rovira II, Allen M, Springer DA, et al. (2013) The physiological role of mitochondrial calcium revealed by mice lacking the mitochondrial calcium uniporter (MCU). *Nat Cell Biol* **15**: 1464–1472
- Pendin D, Greotti E, Pozzan T (2014) The elusive importance of being a mitochondrial Ca²⁺ uniporter. *Cell Calcium* **55**: 139–145
- Perocchi F, Gohil VM, Girgis HS, Bao XR, McCombs JE, Palmer AE, Mootha VK (2010) MICU1 encodes a mitochondrial EF hand protein required for Ca²⁺ uptake. *Nature* **467**: 291–296
- Pittis AA, Goh V, Cebrian-Serrano A, Wettmarshausen J, Perocchi F, Gabaldón T (2020) Discovery of EMRE in fungi resolves the true evolutionary history of the mitochondrial calcium uniporter. *Nat Commun* **11**: 4031
- Prudent J, Popgeorgiev N, Bonneau B, Thibaut J, Gadet R, Lopez J, Gonzalo P, Rimokh R, Manon S, Houart C, et al. (2013) Bcl-wav and the mitochondrial calcium uniporter drive gastrula morphogenesis in zebrafish. *Nat Commun* **4**: 2330
- Raffaello A, De Stefani D, Sabbadin D, Teardo E, Merli G, Picard A, Checchetto V, Moro S, Szabò I, Rizzuto R (2013) The mitochondrial calcium uniporter is a multimer that can include a dominant-negative pore-forming subunit. *EMBO J* **32**: 2362–2376
- Rasmussen TP, Wu Y, Joiner MA, Koval OM, Wilson NR, Luczak ED, Wang Q, Chen B, Gao Z, Zhu Z, et al. (2015) Inhibition of MCU forces extramitochondrial adaptations governing physiological and pathological stress responses in heart. *Proc Natl Acad Sci USA* **112**: 9129–9134
- Resentini F, Grenzi M, Ancora D, Cademartori M, Luoni L, Franco M, Bassi A, Bonza MC, Costa A (2021a) Simultaneous imaging of ER and cytosolic Ca²⁺ dynamics reveals long-distance ER Ca²⁺ waves in plants. *Plant Physiol* **187**: 603–617
- Resentini F, Ruberti C, Grenzi M, Bonza MC, Costa A (2021b) The signatures of organellar calcium. *Plant Physiol* **187**: 1985–2004
- Ruan J, Zhou Y, Zhou M, Yan J, Khurshid M, Weng W, Cheng J, Zhang K (2019) Jasmonic acid signaling pathway in plants. *Int J Mol Sci* **20**: 2479
- Sancak Y, Markhard AL, Kitami T, Kovács-Bogdán E, Kamer KJ, Udeshi ND, Carr SA, Chaudhuri D, Clapham DE, Li AA, et al. (2013) EMRE is an essential component of the mitochondrial calcium uniporter complex. *Science* **342**: 1379–1382
- Schaller A, Stintzi A (2009) Enzymes in jasmonate biosynthesis – Structure, function, regulation. *Phytochemistry* **70**: 1532–1538
- Schiefelbein JW, Shipley A, Rowse P (1992) Calcium influx at the tip of growing root-hair cells of *Arabidopsis thaliana*. *Planta* **187**: 455–459
- Schmittgen TD, Livak KJ (2008) Analyzing real-time PCR data by the comparative C(T) method. *Nat Protoc* **3**: 1101–1108
- Schoenaers S, Balcerowicz D, Costa A, Vissenberg K (2017) The kinase ERULUS controls pollen tube targeting and growth in *Arabidopsis thaliana*. *Front Plant Sci* **8**: 1942
- Schönknecht G (2013) Calcium signals from the vacuole. *Plants (Basel)* **2**: 589–614
- Schwarzländer M, Murphy MP, Duchon MR, Logan DC, Fricker MD, Halestrap AP, Müller FL, Rizzuto R, Dick TP, Meyer AJ, et al (2012) Mitochondrial “flashes”: a radical concept rephined. *Trends Cell Biol* **22**: 503–508
- Selles B, Michaud C, Xiong T-C, Leblanc O, Ingouff M (2018) *Arabidopsis* pollen tube germination and growth depend on the mitochondrial calcium uniporter complex. *New Phytol* **219**: 58–65
- Sello S, Moscattiello R, Mehlmer N, Leonardelli M, Carraretto L, Cortese E, Zanella FG, Baldan B, Szabò I, Voithknecht UC, et al. (2018) Chloroplast Ca²⁺ fluxes into and across thylakoids revealed by thylakoid-targeted aequorin probes. *Plant Physiol* **177**: 38–51
- Senkler J, Senkler M, Eubel H, Hildebrandt T, Lengwens C, Schertl P, Schwarzländer M, Wagner S, Wittig I, Braun HP (2017) The mitochondrial complexome of *Arabidopsis thaliana*. *Plant J* **89**: 1079–1092
- Shan X, Wang J, Chua L, Jiang D, Peng W, Xie D (2011) The role of *Arabidopsis* Rubisco activase in jasmonate-induced leaf senescence. *Plant Physiol* **155**: 751–764
- Shkolnik D, Nuriel R, Bonza MC, Costa A, Fromm H (2018) MIZ1 regulates ECA1 to generate a slow, long-distance phloem-transmitted Ca²⁺ signal essential for root water tracking in *Arabidopsis*. *Proc Natl Acad Sci USA* **115**: 8031–8036
- Smirnova E, Marquis V, Poirier L, Aubert Y, Zumsteg J, Ménard R, Miesch L, Heitz T (2017) Jasmonic acid oxidase 2 hydroxylates jasmonic acid and represses basal defense and resistance responses against *Botrytis cinerea* infection. *Mol Plant* **10**: 1159–1173
- Sparagna GC, Gunter KK, Sheu SS, Gunter TE (1995) Mitochondrial calcium uptake from physiological-type pulses of calcium. A description of the rapid uptake mode. *J Biol Chem* **270**: 27510–27515
- Sparkes IA, Runions J, Kearns A, Hawes C (2006) Rapid, transient expression of fluorescent fusion proteins in tobacco plants and generation of stably transformed plants. *Nat Protoc* **1**: 2019–2025
- Stael S, Wurzingger B, Mair A, Mehlmer N, Voithknecht UC, Teige M (2012) Plant organellar calcium signalling: an emerging field. *J Exp Bot* **63**: 1525–1542
- Stenzel I, Hause B, Miersch O, Kurz T, Maucher H, Weichert H, Ziegler J, Feussner I, Wasternack C (2003) Jasmonate biosynthesis and the allene oxide cyclase family of *Arabidopsis thaliana*. *Plant Mol Biol* **51**: 895–911
- Sun Q, Yu Y, Wan S, Zhao F, Hao Y (2010) Extracellular and intracellular calcium both involved in the jasmonic acid induced calcium mobilization in *Arabidopsis thaliana*. *Agric Sci China* **9**: 497–503
- Tamura K, Stecher G, Peterson D, Filipowski A, Kumar S (2013) MEGA6: molecular evolutionary genetics analysis version 6.0. *Mol Biol Evol* **30**: 2725–2729
- Teardo E, Carraretto L, De Bortoli S, Costa A, Behera S, Wagner R, Lo Schiavo F, Formentin E, Szabo I (2015) Alternative splicing-mediated targeting of the *Arabidopsis* GLUTAMATE RECEPTOR3.5 to mitochondria affects organelle morphology. *Plant Physiol* **167**: 216–227
- Teardo E, Carraretto L, Moscattiello R, Cortese E, Vicario M, Festa M, Maso L, Bortoli SD, Cali T, Voithknecht UC, et al. (2019) A chloroplast-localized mitochondrial calcium uniporter transduces osmotic stress in *Arabidopsis*. *Nat Plants* **5**: 581–588
- Teardo E, Carraretto L, Wagner S, Formentin E, Behera S, Bortoli SD, Larosa V, Fuchs P, Schiavo FL, Raffaello A, et al. (2017) Physiological characterization of a plant mitochondrial calcium uniporter *in vitro* and *in vivo*. *Plant Physiol* **173**: 1355–1370
- Thor K, Jiang S, Michard E, George J, Scherzer S, Huang S, Dindas J, Derbyshire P, Leitão N, DeFalco TA, et al. (2020) The calcium-permeable channel OSCA1.3 regulates plant stomatal immunity. *Nature* **585**: 569–573
- Tian W, Hou C, Ren Z, Wang C, Zhao F, Dahlbeck D, Hu S, Zhang L, Niu Q, Li L, et al. (2019) A calmodulin-gated calcium channel links pathogen patterns to plant immunity. *Nature* **572**: 131–135
- Toyota M, Spencer D, Sawai-Toyota S, Jiaqi W, Zhang T, Koo AJ, Howe GA, Gilroy S (2018) Glutamate triggers long-distance, calcium-based plant defense signaling. *Science* **361**: 1112–1115
- Tripathi D, Zhang T, Koo AJ, Stacey G, Tanaka K (2018) Extracellular ATP acts on jasmonate signaling to reinforce plant defense. *Plant Physiol* **176**: 511–523
- Tsai MF, Phillips CB, Ranaghan M, Tsai CW, Wu Y, Williams C, Miller C (2016) Dual functions of a small regulatory subunit in the mitochondrial calcium uniporter complex. *Elife* **5**: e15545
- Tufi R, Gleeson TP, von Stockum S, Hewitt VL, Lee JJ, Terriente-Felix A, Sanchez-Martinez A, Ziviani E, Whitworth AJ (2019) Comprehensive genetic characterization of mitochondrial Ca²⁺ uniporter components reveals their different physiological requirements *in vivo*. *Cell Rep* **27**: 1541–1550.e5
- Van Aken O, De Clercq I, Ivanova A, Law SR, Van Breusegem F, Millar AH, Whelan J (2016) Mitochondrial and chloroplast stress responses are modulated in distinct touch and chemical inhibition phases. *Plant Physiol* **171**: 2150–2165

- Van Aken O, Whelan J** (2012) Comparison of transcriptional changes to chloroplast and mitochondrial perturbations reveals common and specific responses in *Arabidopsis*. *Front Plant Sci* **3**: 281
- Van Moerkercke A, Duncan O, Zander M, Šimura J, Broda M, Vanden Bossche R, Lewsey MG, Lama S, Singh KB, Ljung K, et al** (2019) A MYC2/MYC3/MYC4-dependent transcription factor network regulates water spray-responsive gene expression and jasmonate levels. *Proc Natl Acad Sci USA* **116**: 23345–23356
- Vasington FD, Murphy JV** (1962) Ca ion uptake by rat kidney mitochondria and its dependence on respiration and phosphorylation. *J Biol Chem* **237**: 2670–2677
- Völkner C, Holzner LJ, Day PM, Ashok AD, de Vries J, Bölter B, Kunz HH** (2021) Two plastid POLLUX ion channel-like proteins are required for stress-triggered stromal Ca²⁺ release. *Plant Physiol* **187**: 2110–2125
- Wagner S, Behera S, De Bortoli S, Logan DC, Fuchs P, Carraretto L, Teardo E, Cendron L, Nietzel T, Füßl M, et al.** (2015) The EF-Hand Ca²⁺ binding protein MICU choreographs mitochondrial Ca²⁺ dynamics in *Arabidopsis*. *Plant Cell* **27**: 3190–3212
- Wagner S, De Bortoli S, Schwarzländer M, Szabó I** (2016) Regulation of mitochondrial calcium in plants versus animals. *J Exp Bot* **67**: 3809–3829
- Wagner S, Steinbeck J, Fuchs P, Lichtenauer S, Elsasser M, Schippers JHM, Nietzel T, Ruberti C, Van Aken O, Meyer AJ, et al** (2019). Multiparametric real-time sensing of cytosolic physiology links hypoxia responses to mitochondrial electron transport. *New Phytol* **224**: 1668–1684
- Wang Y, Nguyen NX, She J, Zeng W, Yang Y, Bai X, Jiang Y** (2019) Structural mechanism of EMRE-dependent gating of the human mitochondrial calcium uniporter. *Cell* **177**: 1252–1261.e13
- Wasternack C** (2007) Jasmonates: an update on biosynthesis, signal transduction and action in plant stress response, growth and development. *Ann Bot* **100**: 681–697
- Weinl S, Held K, Schlücking K, Steinhorst L, Kuhlert S, Hippler M, Kudla J** (2008) A plastid protein crucial for Ca²⁺-regulated stomatal responses. *New Phytol* **179**: 675–686
- White PJ, Broadley MR** (2003) Calcium in plants. *Ann Bot* **92**: 487–511
- Wudick MM, Portes MT, Michard E, Rosas-Santiago P, Lizzio MA, Nunes CO, Campos C, Santa Cruz Damineli D, Carvalho JC, Lima PT, et al.** (2018) CORNICHON sorting and regulation of GLR channels underlie pollen tube Ca²⁺ homeostasis. *Science* **360**: 533–536
- Xu S, Chisholm AD** (2014) *C. elegans* epidermal wounding induces a mitochondrial ROS burst that promotes wound repair. *Dev Cell* **31**: 48–60
- Xu Y, Berkowitz O, Narsai R, Clercq ID, Hooi M, Bulone V, Breusegem FV, Whelan J, Wang Y** (2019) Mitochondrial function modulates touch signalling in *Arabidopsis thaliana*. *Plant J* **97**: 623–645
- Yamanaka T, Nakagawa Y, Mori K, Nakano M, Imamura T, Kataoka H, Terashima A, Iida K, Kojima I, Katagiri T, et al.** (2010) MCA1 and MCA2 that mediate Ca²⁺ uptake have distinct and overlapping roles in *Arabidopsis*. *Plant Physiol* **152**: 1284–1296
- Yan C, Fan M, Yang M, Zhao J, Zhang W, Su Y, Xiao L, Deng H, Xie D** (2018) Injury activates Ca²⁺/calmodulin-dependent phosphorylation of JAV1-JAZ8-WRKY51 complex for jasmonate biosynthesis. *Mol Cell* **70**: 136–149.e7
- Yoshimura K, Iida K, Iida H** (2021) MCAs in *Arabidopsis* are Ca²⁺-permeable mechanosensitive channels inherently sensitive to membrane tension. *Nat Commun* **12**: 6074
- Yuan F, Yang H, Xue Y, Kong D, Ye R, Li C, Zhang J, Theprungsirikul L, Shrift T, Krichilsky B, et al.** (2014) OSCA1 mediates osmotic-stress-evoked Ca²⁺ increases vital for osmosensing in *Arabidopsis*. *Nature* **514**: 367–371
- Zhang B, Van Aken O, Thatcher L, De Clercq I, Duncan O, Law SR, Murcha MW, van der Merwe M, Seifi HS, Carrie C, et al.** (2014) The mitochondrial outer membrane AAA ATPase AtOM66 affects cell death and pathogen resistance in *Arabidopsis thaliana*. *Plant J* **80**: 709–727
- Zhang Y, Turner JG** (2008) Wound-induced endogenous jasmonates stunt plant growth by inhibiting mitosis. *PLoS One* **3**: e3699
- Zottini M, Zannoni D** (1993) The use of fura-2 fluorescence to monitor the movement of free calcium ions into the matrix of plant mitochondria (*Pisum sativum* and *Helianthus tuberosus*). *Plant Physiol* **102**: 573–578